Journal of Marine Research, 56, 157–196, 1998

The salt finger amplitude in unbounded T-S gradient layers

by Melvin E. Stern[1] and Timour Radko[1]

ABSTRACT

Finite amplitude numerical calculations are made for a completely unbounded salt finger domain whose overall vertical "property" gradients ($\overline{T}_z$ and $\overline{S}_z$) are uniform and remain unaltered in time. For diffusivity ratio $\tau = \kappa_S/\kappa_T = O(1)$, Prandtl number $\nu/\kappa_T \gg 1$, and density ratio $R = \overline{T}_z/\overline{S}_z > 1$ this regime corresponds to a "double gradient" sugar (S) − salt (T) experiment. Two-dimensional pseudo-spectral calculations are made in the vicinity of the minimum critical condition for salt finger instability, viz., small $\epsilon \equiv (R\tau)^{-1} - 1 > 0$; the allowed spectrum includes the fastest growing wave of linear theory. When the vertical wavelength of the fundamental Fourier component is systematically increased the solution changes from a single steady vertical mode to a multi-modal statistically steady chaotic state. Each of the long vertical modes can be amplified by the (unchanging overall) gradient $\overline{S}_z$, and can be stabilized by the induced vertical T, S gradients on the same scale as the modes; nonlinear triad interactions in the $T - S$ equations can also lead to amplitude equilibration even though ϵ, κ_T/ν, and the Reynolds number are extremely small. When subharmonics of the horizonal wavelength of maximum growth are introduced into the numerical calculations the new wave amplifies (via $\overline{S}_z$) and produces a quantitative change in the time average fluxes.

Experimentally testable values of heat flux and rms horizontal T-fluctuations are computed in the range $2.8 > R > 1.6$ for $\tau = 1/3$. Asymptotic similarity laws $\epsilon \to 0$ are also presented.

1. Introduction

Previous theoretical and experimental studies related to salt finger convection in the ocean have mainly considered a so called "fully developed" state consisting of two very deep fluid layers whose given uniform temperatures and salinities (or solute concentrations) determine the equilibrium thickness of a relatively thin intervening high "gradient region" containing vertically coherent fingers. The vertical velocity and fluxes produced by these are also determined by the "temperatures" and "salinities" of the deep layers, as well as by the viscosity ν, the thermal diffusivity κ_T, and the salt diffusivity κ_S or $\tau = \kappa_S/\kappa_T$. Although such thin finger regions are sometimes observed (Williams, 1981) in oceanic microstructure measurements, more often (Schmitt *et al.,* 1987) the thickness of the associated vertical gradient region is much too large for consistency with the aforementioned "fully developed" laboratory regime, and therefore the fingers in that oceanic region could only be coherent over a small fraction of the entire gradient region. In this paper we consider what happens when this region is vertically *unbounded,* with initially

1. Department of Oceanography, The Florida State University, Tallahassee, Florida, 32306-4320, U.S.A.

given uniform vertical solute *gradients* whose values determine such average quantities as heat flux and rms concentration fluctuations.

Such deep gradient layers have been realized in double gradient laboratory experiments (e.g., Stern and Turner, 1969; Taylor, 1993) using two *solutes* (such as sugar and salt with $\tau = O(1) < 1$); these "(S, T) properties" are analogous to ordinary temperatures and salinities. These properties are converted to density fluctuations using the equation of state, and it is convenient to absorb the expansion and contraction coefficients into new (T, S) variables, so that henceforth these ("temperatures, salinities") correspond to *density* or buoyancy fluctuations in the Boussinesq equations. Nearly uniform vertical gradients with $\overline{T}_z > \overline{S}_z > 0$ have been produced in a deep tank by the "double bucket" technique, wherein a pure T-solution (e.g., salt) in one bucket is connected by a capillary siphon to a second bucket at the *same* elevation containing a pure S-solution (e.g., sugar) of lesser density. The latter is connected by a siphon to the *lower* lying bottom of the experimental tank, so that when both siphons are opened pure S-water enters the tank, and pure T-water flows into the S-bucket where it is completely mixed by a mechanical stirrer. This slightly diluted mixture then enters the tank bottom underneath the slightly less dense S-water, and so on until the tank is filled to a known depth with pure S-water at the top, pure T-water at the bottom, and with nearly uniform $\overline{S}_z$, $\overline{T}_z$ gradients in-between. For suitable filling conditions and moderately large $R = \overline{T}_z/\overline{S}_z$ upgoing and downgoing salt fingers form and occupy the entire tank. Despite the predominant vertical structure and square planform (Shirtcliffe and Turner, 1970), wiggles and bifurcations are observed in the fingers, as well as planform irregularity in the horizontal. As we shall see, the explanation of these features, as well as the prediction of average quantities, pose a potentially tractable statistical mechanical problem, even when the finger Reynolds number is extraordinarily small.

The asymptotic regime relevant to the foregoing experiment consists of an *unbounded* fluid with

$$\frac{\nu}{\kappa_T} \to \infty, \qquad \tau = \frac{\kappa_S}{\kappa_T} = O(1), \qquad R - 1 = O(1) \tag{1a}$$

$$0 < \epsilon \equiv \frac{1}{\tau R} - 1 = O(1) \tag{1b}$$

where $R = \overline{T}_z/\overline{S}_z$ is the density ratio of the undisturbed state. It is well known (Stern, 1975, p. 193) that such an unbounded model has an exact nonlinear solution for all Prandtl numbers (ν/κ_T) in which the amplitude of a depth (z) *independent* normal mode continually increases with time, so that it never reaches a steady state. Thus there must be other effects which intervene to produce $\partial/\partial z \neq 0$, and to bring about equilibrium. In the oceanic context, Kunze (1994) suggests that ambient large-scale vertical shear can do this by disrupting the fingers, but in the cited laboratory experiments there is no such external current, and various secondary instabilities (Holyer, 1984) have been proposed; these draw their energy from the steady depth independent field of salt fingers which arise from the

primary ($\overline{S}_z$, $\overline{T}_z$) instability. However, the equilibrium amplitude of that finger field has yet to be fully explained, despite the insights gained by the finite amplitude theories of Joyce (1982) and Proctor and Holyer (1986). These authors develop a weak nonlinear theory for fingers with a small but finite aspect ratio $\delta = d/H$, where d is the canonical finger width (defined later) and H is the finite vertical separation of boundaries at which either flux or (T, S) conditions are specified. Moreover the expansion technique requires the horizontal wavelength to be in the vicinity of the one with *zero* growth rate, rather than maximal. It is then shown that the slightly amplifying mode equilibrates as the result of its alteration of the mean ($\overline{T}_z$, $\overline{S}_z$) fields, in a manner similar to that which occurs in classical Rayleigh-Benard convection (Malkus and Veronis, 1958) between two parallel boundaries. Proctor and Holyer (1986) also show that *two* dimensional "sheets" rather than fingers are stable, and thus the observed (Shirtcliffe and Turner, 1970) square planform is as yet unexplained.

Numerical calculations for the evolution of the *fastest* growing two dimensional mode have been made for the case of a *thin heat*-salt gradient region (Shen and Veronis, 1997), but equilibrium was not reached for this very large amplitude case. Also for the finite gradient layer, Özgökmen *et al.* (1998), achieved two dimensional equilibrium in a long numerical calculations (using Prandtl and Lewis numbers much different from heat-salt or salt-sugar). The unbounded gradient case model has been considered by Whitfield *et al.* (1989) for τ in the range (Eq. (1)) of sugar/salt experiments, but the Prandtl number was much smaller; the numerically computed statistically steady state [their Fig. 6] consisted of round blobs of salinity (and streamfunction) rather than the vertically elongated finger structure observed in all cited laboratory experiments.

We propose to obtain a better understanding of the amplitude and structure of salt fingers by focusing on a simpler parametric regime (Eq. (1)), but one which is still realizable. The statistically steady state arising from a disturbance spectrum which includes the fastest growing horizontal wavelength will first be computed for an unbounded sugar/salt gradient when ϵ in Eq. (1) is small but finite, or when R is slightly less than the minimum critical value for stability of the undisturbed vertical gradients.

Before turning to the relevant two-dimensional numerical calculations (Section 3a) we note (Section 2) that in the marginally stable limit, as $\epsilon \to 0$, the maximum (linear) growth rate shifts to slightly longer ($\epsilon^{-1/4}d$) horizontal wavelengths, and all relatively long vertical wavelengths have virtually the same linear growth rate. A rescaling (Section 2b) of the nonlinear high Prandtl number equations then leads to a further simplified asymptotic ($\epsilon \to 0$) set of equations for the three dimensional temperature field (Eqs. 17–18b). These asymptotic equations will be useful in interpreting the main results of this paper, provided by the finite ϵ numerical solutions; but for practical computational reasons it is difficult to make the latter for too small values of ϵ; furthermore, our ultimate interest is in the larger ϵ achieved in previous laboratory experiments.

It is also of interest to compare some of the numerical results of Section 3a with an approximate analytic theory; this is similar to that of Joyce (1982), except that our calculation is based on a single mode truncation for the *fastest* growing wave when $\epsilon \to 0$.

The result [Appendix] is in acceptable agreement with the (exact) numerics *only* when the fundamental Fourier wavelength $2\pi/\mu$ in the vertical direction is a small multiple of the finger width. When μ is decreased many long vertical wavelengths amplify (for reasons previously mentioned), and the numerically computed steady state amplitude becomes much larger than the single mode approximation, even though $\epsilon \ll 1$. With further decrease of μ the solutions of the equations of motion become very irregular in time, and thus the single mode truncation, or indeed any "weakly" nonlinear theory, is qualitatively unable to describe long salt fingers even when the Reynolds number is extraordinarily small. The long time integrations (Section 3b) of the high Prandtl number equations for $\epsilon = 0.0714$, $\tau = \frac{1}{3}$ and various $\mu \ll 1$, enable us to estimate the time average heat flux and rms temperature fluctuation. Section 4 reveals that these chaotic two dimensional solutions undergo substantial quantitative change when subject to small amplitude disturbances with *horizontal* wavelengths longer than the one of maximum growth. These are also amplified (by $\overline{S}_z, \overline{T}_z$) because of their long vertical wavelength, and they are therefore not Holyer (1984) or "collective" instabilities. In Section 5 the calculations are extended to larger ϵ, and the corresponding heat flux is presented. The reader who is less interested in the mathematical details may skip from Eq. (4b) to (10a), and also skip Section 2b.

Although the oceanic values of $\tau = 10^{-2}$, $\nu/\kappa_T = 7$ are significantly different from the sugar-salt values, the laboratory experiments for the latter case have proven extremely suggestive of some ocean observations. We particularly refer to those experiments (Turner, 1978) involving large-scale *lateral* intrusions, and accompanied by salt fingers in regions of enhanced vertical gradients. Qualitatively similar intrusions seem to occur in an important phase of the large-scale mixing process, wherein shear straining of $T - S$ variations on isopycnal surfaces produce the enhanced vertical gradients on which significant finger and convective microstructure can occur. Such effects are strongly implicated in Meddies (Ruddick, 1992), and in the ice covered Arctic where warm salty Atlantic water intrudes (Carmack *et al.,* 1995).

2. Asymptotic formulations

a. Large Prandtl number

The Boussinesq equations of motion will be nondimensionalized using the conventional finger width $d = (\kappa_T \nu / g\overline{T}_z)^{1/4}$ as the length scale; $\overline{T}_z d$ is the scale for both the total "temperature" *deviation* $(T'(x, y, z, t) + \theta(z, t))$ and the total "salinity" deviation $(S' + \sigma(z, t))$ from their respective undisturbed values $(\overline{T}, \overline{S})$; κ_T/d is the velocity scale; d^2/κ_T is the time scale, and $\nu\kappa_T/d^2$ is the pressure scale. When Eq. (1) applies the nonlinear inertial terms $(O(\kappa_T/\nu) \ll 1)$ are negligible and the nondimensional Boussinesq equations reduce to

$$0 = -\nabla p + \nabla^2 \mathbf{V} + (T' - S')\mathbf{K}, \tag{2a}$$

$$\nabla \cdot \mathbf{V} = 0, \tag{2b}$$

$$\frac{d}{dt}[T'(x, y, z, t) + \theta(z, t)] + w = \nabla^2(T' + \theta), \tag{3a}$$

$$\tau^{-1}\frac{d}{dt}[S'(x, y, z, t) + \sigma(z, t)] + \tau^{-1}R^{-1}w = \nabla^2(S' + \sigma) \tag{3b}$$

where (w, u, v) are the (z, x, y) components of $\mathbf{V}$, and $\mathbf{K}$ is the vertical unit vector. In these equations the undisturbed temperature gradient is unity, and the undisturbed salinity gradient is $R^{-1} < 1$. The dimensional convective heat flux equals $\kappa_T\overline{T}_z$ times the nondimensional value, and the dimensional rms T' equals $(\overline{T}_z d)$ times the nondimensional value obtained from (2a)–(3b).

Let us look for solutions which are spatially periodic in (x, y, z) domains extending to infinity. If $\overline{(\ )}$ denotes a horizontal average and $\langle\ \rangle$ a vertical average then

$$\overline{T}' = 0 = \overline{S}' = \overline{w}, \qquad 0 = \langle\theta\rangle = \langle\sigma\rangle,$$

the horizontal averages of (3a,b) give the "mean field" equations

$$\frac{\partial\theta}{\partial t} + \frac{\partial}{\partial z}\overline{wT}' = \frac{\partial^2\theta}{\partial z^2}, \tag{4a}$$

$$\tau^{-1}\left(\frac{\partial\sigma}{\partial t} + \frac{\partial}{\partial z}\overline{wS}'\right) = \frac{\partial^2\sigma}{\partial z^2}. \tag{4b}$$

When the latter are subtracted from (3a,b) the results are

$$\mathbf{D}T' + w = -w\frac{\partial\theta}{\partial z} - \left(\nabla\cdot(\mathbf{V}T') - \frac{\partial}{\partial z}\overline{wT}'\right), \tag{5a}$$

$$\mathbf{D}_\tau S' + R^{-1}\tau^{-1}w = -\tau^{-1}w\frac{\partial\sigma}{\partial z} - \tau^{-1}\left(\nabla\cdot(VS') - \frac{\partial}{\partial z}\overline{wS}'\right), \tag{5b}$$

where

$$\mathbf{D} \equiv \frac{\partial}{\partial t} - \nabla^2, \tag{6a}$$

$$\mathbf{D}_\tau = \frac{1}{\tau}\frac{\partial}{\partial t} - \nabla^2, \tag{6b}$$

and we shall also use

$$\nabla_2^2 = \nabla^2 - \frac{\partial^2}{\partial z^2} \equiv \frac{\partial^2}{\partial x^2} + \frac{\partial^2}{\partial y^2}. \tag{6c}$$

By eliminating the horizontal pressure gradients from (2a) we obtain the vorticity equation (useful in the three dimensional problem):

$$\partial u/\partial y - \partial v/\partial x = 0. \tag{7a}$$

Eqs. (2a,b) also give

$$\nabla^4 w = \nabla_2^2(S' - T'), \tag{7b}$$

and when

$$\rho' = S' - T' \tag{7c}$$

is eliminated using (5a) and (5b) the result may be expressed as

$$\mathbf{L}\left(\frac{\partial}{\partial t}, \frac{\partial}{\partial x}, \frac{\partial}{\partial y}, \frac{\partial}{\partial z}\right) w = N + Q \tag{8}$$

where the linear operator in this equation is

$$\mathbf{L}\left(\frac{\partial}{\partial t}, \frac{\partial}{\partial x}, \frac{\partial}{\partial y}, \frac{\partial}{\partial z}\right) \equiv \mathbf{D}_\tau \mathbf{D} \nabla^4 - \left[(R^{-1}\tau^{-1} - 1)\nabla^2 + \tau^{-1}(1 - R^{-1})\frac{\partial}{\partial t}\right]\nabla_2^2. \tag{9a}$$

There are two different nonlinear terms in Eq. (8), one of which, due to the *mean field* (θ, σ) modification, is

$$Q = -\tau^{-1}\mathbf{D}\nabla_2^2\left(w\frac{\partial \sigma}{\partial z}\right) + \mathbf{D}_\tau \nabla_2^2\left(w\frac{\partial \theta}{\partial z}\right).$$

Since the last term in (5a) and (5b) is independent of (x, y), the value of the other nonlinear term is

$$N = -\tau^{-1}\mathbf{D}\nabla_2^2\nabla \cdot (\mathbf{V}S') + \mathbf{D}_\tau \nabla_2^2 \nabla \cdot \mathbf{V}T'. \tag{9b}$$

The well-known solution of the linear problem $\mathbf{L}(w) = 0$ for w, T', S' gives the eigenfunctions as the product of $e^{\lambda_m t}$ with

$$(w_m, T_m, S_m) \propto \sin kx \cos \ell y \cos mz, \tag{10a}$$

and thus the eigenvalue equation $\mathbf{L}(w) = 0$ for the growth rate λ_m is

$$(\lambda_m + k_0^2 + m^2)[\lambda_m + \tau(k_0^2 + m^2)](k_0^2 + m^2)^2 + \lambda_m k_0^2(1 - R^{-1}) - k_0^2(k_0^2 + m^2)\tau\epsilon = 0.$$

The $\epsilon \to 0$ limit for $\lambda_m \to 0$ is

$$\lambda_m = \frac{\epsilon\tau k_0^2(k_0^2 + m^2) - \tau(k_0^2 + m^2)^4}{(k_0^2 + m^2)^3(1 + \tau) + k_0^2(1 - R^{-1})} + \ldots,$$

and with the wavenumber rescaling given by

$$(k, \ell, m) \equiv \epsilon^{1/4}(\hat{k}, \hat{\ell}, \hat{m}), \tag{10b}$$

$$k_0^2 \equiv k^2 + \ell^2, \qquad \hat{k}_0^2 \equiv \hat{k}^2 + \hat{\ell}^2 \tag{10c}$$

the leading term in the ϵ-expansion is

$$\lambda_m = \tau\epsilon^{3/2}(\hat{k}_0^2 + \hat{m}^2)\frac{[\hat{k}_0^2 - (\hat{k}_0^2 + \hat{m}^2)^3]}{(1-\tau)\hat{k}_0^2} + \ldots, \tag{11}$$

where the rescaled wavenumbers are $O(1)$. In this $\epsilon \to 0$ limit $R^{-1}\tau^{-1} \approx 1$, and the limit of the T_m, S_m eigenfunctions (10a), obtained from the linearization of (5), (6), reduce to

$$T_m = S_m = -\frac{w_m}{k_0^2 + m^2} = -\frac{w_m}{(\hat{k}_0^2 + \hat{m}^2)\epsilon^{1/2}}. \tag{12}$$

For "thin" fingers with *finite* $m^2/k_0^2 \ll 1$, the maximum of (11) and the corresponding wave number are

$$\max \lambda_m = \sqrt{\frac{4}{27}}\frac{\tau}{1-\tau}\epsilon^{3/2}, \qquad \hat{k}_0^2 = \frac{1}{\sqrt{3}}. \tag{13}$$

Note that wave number $2\hat{k}_0$ is damped, but $\hat{k}_0/2$ is not if $\hat{m}$ is small. It should be emphasized that if $\tau < 1 = O(1)$ is fixed as $\epsilon \to 0$ then $R = [\tau(1+\epsilon)]^{-1}$ must be increased accordingly.

When $\epsilon \to 0$ the finite amplitude of the disturbance should also vanish, and the solution of a steady truncated version of these equations (Appendix) will be compared with the numerical solutions of the exact two dimensional equations in Section 3a. But the steady solutions will be found to be highly unstable, and our focus will be on the multi-modal time-dependent solutions.

b. The nonlinear $\epsilon \to 0$ equations

Before turning to these calculations it is instructive to consider the $\epsilon \to 0$ limit to the high Prandtl number equations. When Eq. (5a) is subtracted from (5b), and (7c) is used we obtain a "density equation"

$$-\nabla^2\rho' + \frac{\partial}{\partial t}\left(\frac{S'}{\tau} - T'\right) + \epsilon w = -w\left(\tau^{-1}\frac{\partial\sigma}{\partial z} - \frac{\partial\theta}{\partial z}\right) + G, \tag{14a}$$

$$G \equiv -\tau^{-1}\left(\nabla\cdot S'\mathbf{V} - \frac{\partial}{\partial z}\overline{S'w}\right) + \nabla\cdot T'\mathbf{V} - \frac{\partial}{\partial z}\overline{T'w}, \tag{14b}$$

in which the crucial term ϵw is reduced by a factor ϵ relative to its value (w) in (5a). When $\epsilon \to 0$ the first two terms in Eq. (12) suggest that $\rho' = S' - T' \ll 0$ (S'), and Eq. (13) suggests that $\partial/\partial t \sim \epsilon^{3/2}$. Accordingly, all variables in (14a) are now transformed using $\epsilon^{-3/2}$ as the time scale, $x \sim \epsilon^{-1/4}$ as the horizontal scale (from 10b), but a much larger z-scale for the finite amplitude fingers is anticipated. Since the nonlinear mean field terms in Eq. (14a) are expected (for stabilization) to be of the same order as ϵw we have $\partial\theta/\partial z \sim \epsilon \sim \partial\sigma/\partial z$, and from the diffusive advective heat balance (4a) $\overline{wT}' \sim \partial\theta/\partial z \sim \epsilon$ is obtained. The linear terms in Eq. (5a) give $w \sim \nabla^2 T' \sim \partial^2 T'/\partial x^2 \sim \epsilon^{1/2} T'$, and combining the foregoing results yields $w^2\epsilon^{-1/2} \sim \epsilon$, $w \sim \epsilon^{3/4}$, and $\epsilon^{1/4} \sim T' \sim S'$. A final assertion is that the nonlinear G term is of the same order as all the other terms in (14a), e.g., $\partial T'/\partial t$; this is equivalent to requiring $\partial/\partial t \sim w\partial/\partial z$, or $\epsilon^{3/2} \sim \epsilon^{3/4}\partial/\partial z$, giving $z \sim \epsilon^{-3/4}$ for the "vertical scale" of the fingers. From the continuity requirement $\partial u/\partial x \sim \partial w/\partial z$, the horizontal velocity $u \sim \epsilon^{-1/4}\epsilon^{3/4}\epsilon^{3/4} = \epsilon^{5/4}$ is obtained, and Eq. (7b) gives the density $\rho' \sim \partial^2 w/\partial x^2 \sim \epsilon^{1/2}\epsilon^{3/4}$.

These anticipated balances lead to the following formal transformations of the variables in the temperature, salinity, momentum, and continuity equations. Let

$$(x, y) = \epsilon^{-1/4}(x_1, y_1), \qquad z = \epsilon^{-3/4} z_1, \qquad t = t^{-3/2} t_1 \tag{15a}$$

$$w = \epsilon^{3/4} w_1, \qquad (u, v) = \epsilon^{5/4}(u_1, v_1), \qquad \mathbf{V}_1 \equiv (u_1, v_1, w_1) \tag{15b}$$

$$(T', S') = \epsilon^{1/4}(T_1, S_1), \qquad (\partial\theta/\partial z, \partial\sigma/\partial z) = \epsilon(\beta_T(z_1, t_1), \beta_s) \tag{15c}$$

$$\rho' = \epsilon^{5/4}\rho_1, \quad \nabla_h^2 = \partial^2/\partial x_1^2 + \partial^2/\partial y_1^2, \quad \nabla_3 = (\partial/\partial x_1, \partial/\partial y_1, \partial/\partial z_1). \tag{15d}$$

The result of taking the $\epsilon \to 0$ limit is as follows. From (5a), (5b), (7b) we get $\nabla_h^2 T_1 = w_1 = \nabla_h^2 S_1$, and $\nabla_h^4 w_1 = \nabla_h^2 \rho_1$; and because of horizontal periodicity these simplify to

$$w_1 = \nabla_n^2 T_1, \qquad S_1 = T_1, \qquad \rho_1 = \nabla_h^2 w_1. \tag{16a}$$

These time *independent* balances constitute "diagnostic" equations, as do Eqs. (7a) and (2b), or

$$\frac{\partial u_1}{\partial y_1} - \frac{\partial v_1}{\partial x_1} = 0, \qquad \frac{\partial u_1}{\partial x_1} + \frac{\partial v_1}{\partial y_1} + \frac{\partial w_1}{\partial z_1} = 0. \tag{16b}$$

When Eq. (16a) is used in the $\epsilon \to 0$ limit of (14a,b), we get the "evolutionary" equation

$$(\tau^{-1} - 1)\left[\frac{\partial T_1}{\partial t_1} + \nabla_3 \cdot (T_1 \mathbf{V}_1) - \frac{\partial}{\partial z_1}(\overline{T_1 w_1})\right] - \nabla_h^6 T_1 + \nabla_h^2 T_1 + (\tau^{-1}\beta_s - \beta_T)\nabla_h^2 T_1 = 0 \tag{17}$$

for the horizontal temperature fluctuation. When the mean field equations (4a, 4b) are

differentiated, and then rescaled, the gradients (β_T, β_S) in (15c) are given by

$$\left(\frac{\partial}{\partial t_1} - \frac{\partial^2}{\partial z_1^2}\right)\beta_T = -\frac{\partial^2}{\partial z_1^2}\overline{T_1\nabla_h^2 T_1}, \tag{18a}$$

$$\left(\frac{\partial}{\partial t_1} - \tau\frac{\partial^2}{\partial z_1^2}\right)\beta_s = -\frac{\partial^2}{\partial z_1^2}\overline{T_1\nabla_n^2 T_1}. \tag{18b}$$

The velocities in Eq. (17) may be eliminated by using Eqs. (16b), the first of which is equivalent to $u_1 = \partial\phi/\partial x$, $v_1 = \partial\phi/\partial y$, and then the second becomes

$$\nabla_h^2\phi + \frac{\partial}{\partial z}\nabla_h^2 T_1 = 0.$$

Because of the horizontal periodicity this reduces to

$$\phi = -\frac{\partial T_1}{\partial z}, \tag{19}$$

and consequently

$$u = -\frac{\partial^2 T_1}{\partial x_1 \partial z_1} \qquad v = -\frac{\partial^2 T_1}{\partial y_1 \partial z_1} \qquad w = \left(\frac{\partial^2}{\partial x_1^2} + \frac{\partial^2}{\partial y_1^2}\right)T_1. \tag{20}$$

Thus we have complete equations (17)–(18) for the three dimensional temperature field, and these are much simpler than Eqs. (2)–(3).

The time dependent equation (17) must be interpreted cautiously since it is not uniformly valid in time, and because the highest z-derivatives have been eliminated; consequently the linear part of (17) does not have a high growth rate cutoff, as does Eq. (11). Likewise the time dependent term in Eqs. (18) may give unreliable long term ($t \gg \epsilon^{-3/2}$) effects when $m \ll 1$ modes are included, because $\partial\beta_T/\partial t_1 \ll 1$ for such modes. Greater significance may therefore be attached to the integral and qualitative properties discussed below.

When (17) is multipied with T_1 and the time average (av) is taken the first three terms separately vanish and we get the important "power integral"

$$\mathrm{av}\langle\overline{(\nabla_h^2\nabla_h T_1)^2}\rangle = \mathrm{av}\langle\overline{(\nabla_h T_1)^2}\,(1 + \tau^{-1}\beta_S - \beta_T)\rangle. \tag{21}$$

The positive definite first term, coming from $\nabla_h^2\rho'$, can be interpreted as a *dissipation* of density (not temperature) fluctuation, and the second term as a *production* due to the vertical flux of heat and the mean fields. The dissipation term, with the *sixth* order horizontal derivative, obviously occurs at smaller scales than the production term. If Eq. (18a) is written in its pre-differentiated (cf. 4a) form $(\partial/\partial t - \partial^2/\partial z^2)\theta_\beta = -\partial/\partial z(T_1\nabla_n^2 T_1)$,

where $\beta_T \equiv \partial\theta_\beta/\partial z_1$, and then multiplied by θ_β, the integrated result is

$$\mathrm{av}\langle\beta_T^2\rangle = -\langle\beta_T\overline{(\nabla T_1)^2}\rangle. \tag{22a}$$

A similar procedure for (18b) gives

$$\mathrm{av}\langle\beta_s^2\rangle = -\tau^{-1}\langle\beta_S\overline{(\nabla T_1)^2}\rangle, \tag{22b}$$

and substitution of these in (21) leads to the further simplification:

$$\mathrm{av}\langle\overline{(\nabla_h^2\nabla_h T_1)^2}\rangle = \mathrm{av}\{\langle\overline{(\nabla_h T_1)^2}\rangle - \langle\beta_s^2\rangle + \langle\beta_T^2\rangle\}. \tag{22c}$$

On purely dimensional grounds, Eqs. (15) suggest that the statistically steady solution of the high Prandtl number equations when $\epsilon \to 0$ should have a nondimensional heat flux proportional to $\epsilon \to 0$, and a nondimensional horizontal temperature fluctuation proportional to $\epsilon^{1/4}$; the corresponding dimensional heat flux and rms temperature are

$$\frac{\mathrm{av}\langle\overline{wT'}\rangle}{\kappa_T\partial\overline{T}/\partial z} = \epsilon C_H(\tau), \tag{23a}$$

$$\frac{\mathrm{av}\langle\overline{(T')^2}\rangle^{1/2}}{\dfrac{\partial\overline{T}}{\partial z}[\kappa_T\nu/(g\overline{T}_z)]^{1/4}} = \epsilon^{1/4}C_T(\tau), \tag{23b}$$

$$\epsilon = \frac{1}{R\tau} - 1 \to 0,$$

where the C are universal functions of $\kappa_S/\kappa_T = O(1)$. In addition the ratio of the buoyancy flux ($w\rho_1$) to the heat flux is proportional to $\epsilon^{5/4}$.

Such laws are predicated on the existence of a *bounded* ensemble of statistically steady solutions when *very large* vertical wavelengths are permitted, a reservation which is nontrivial because we know that there is a particular solution with $\partial/\partial z \equiv 0$ which does *not* reach a finite steady state. It is therefore instructive to point out the ways in which the model can lead to equilibration of the mode with wave number $m_1 = 0$ when other (k_1, ℓ_1, m) modes are present.

Let $\langle T_1\rangle$ denote the average T_1 over an infinite vertical distance, so that this is the amplitude of the Fourier $m_1 = 0$ mode; then the corresponding average of (17) is

$$(\tau^{-1} - 1)\left[\frac{\partial}{\partial t_1}\langle T_1\rangle + \frac{\partial}{\partial x_1}\langle u_1 T_1\rangle + \underset{③}{\frac{\partial}{\partial y}\langle v_1 T_1\rangle}\right] + \underset{①}{(\nabla_h^2 - \nabla_h^6)\langle T_1\rangle} + \underset{②}{\left\langle\left(\frac{\beta_S}{\tau} - \beta_T\right)\nabla_h^2 T_1\right\rangle} = 0. \tag{24}$$

The two terms in ① provide the linear growth rate of a mode whose (x, y, z) wave numbers are $(k_1, \ell_1, 0)$ and term ② can provide a reduction of this growth rate by modifying the mean fields. The two "triad" terms ③ provide a vertically integrated eddy heat conver-

gence by all m-modes which can alter the growth of the $(k_1, \ell_1, 0)$ Fourier mode; e.g., the $(2k_1, 2k_1, m)$ mode interacting with (k_1, k_1, m) (in u_1T_1, etc.) can decrease the $(k_1, k_1, 0)$ component of $\langle T_1 \rangle$ in Eq. (24). This and other effects will appear in the more general field equations considered below.

3. Numerical solutions of the 2D-large Prandtl number equations at small finite ϵ

In the pseudo-spectral calculations given below it is convenient to combine the $T' + \theta$ of Eq. (3a) into $T(x, z, t)$ and $S' + \sigma$ is combined into S; so that in two dimensions the high Prandtl number equations for T, S, and the streamfunction $\psi(x, z, t)$ are

$$\partial T/\partial t + J(\psi, T) + \partial\psi/\partial x = \nabla^2 T, \tag{25a}$$

$$\partial S/\partial t + J(\psi, S) + R^{-1}\partial\psi/\partial x = \tau\nabla^2 S, \tag{25b}$$

$$\nabla^4\psi = \partial(S - T)/\partial x, \tag{25c}$$

where $J = \psi_x T_z - \psi_z T_x$ is the Jacobian. Solutions will be obtained which are periodic in (x, z) with respective fundamental wavelengths $(2\pi/k_0, 2\pi/\mu)$, where henceforth k_0 is the wavenumber of maximum growth rate (e.g., $(\epsilon/3)^{1/4}$ for small ϵ) and μ is an arbitrarily chosen wavenumber which will be systematically decreased to ascertain whether averages of the time dependent solution exist as $\mu \to 0$. The higher vertical wavenumbers are $m \geq \mu$, and the higher horizontal wavenumbers are $k \geq k_0$. In Section 4 the latter condition is relaxed to consider $k < k_0$.

By using a biperiodic grid with (N_x, N_z) points, Eqs. (25) were inverted exactly in Fourier space, and the time integration in Fourier space was done using a fourth order Runge-Kutta scheme. The time step Δt necessary for computational stability is severely limited by the high order of the derivatives in Eq. (9a) but this problem is somewhat alleviated at small ϵ because of the small linear growth rate, Eq. (11). Calculations were performed for various (N_x, N_z); in those calculations for which a steady state was reached the grid point numbers were (32, 32), while for the unsteady ones with smallest μ the values were (16, 256). In Section 5 we will compare results obtained using a dealiased code, with the one used in this section.

For $\tau = 1/3$, $\epsilon = 0.111$, $k_0 = (\epsilon/3)^{1/4}$, $\mu/k_0 = 0.25$ a preliminary run with $\Delta t = 0.05$ and initialized with a normal mode of amplitude 0.1 (for T') gave very good agreement with the growth rate of linear theory up to $t = 50$. We emphasize here that even if T' is initialized with a Fourier mode of the form $\sin\mu z \sin k_0 x$, and even though a "pure sin-z" Fourier series is a possible solution, the *full* code used below calculates the evolution of all harmonics (i.e., *all* the Fourier sine-z and cosine-z terms), such as are inevitably generated by numerical noise. Reference will also be made to various "truncated" codes, one of which suppresses the cosine-z series by setting it to zero after each time step, and another one which suppresses some of the higher k components.

a. Steady state numerical solutions at moderate μ

At moderately small fundamental μ, the evolution of a normal mode with initially small amplitude reached a steady state, as indicated for $\epsilon = 0.111$ (Fig. 1) by the "x" points. These are in fair agreement with the solid curve obtained from the analytical results (Eq. (A7)) derived in the Appendix on the basis of a steady single mode truncation of Eqs. (4a), (4b), (8) when $\epsilon \to 0$; this theoretical approximation is similar to that used by Joyce (1982), except that our results apply to the *fastest* growing $k = k_0$ at the point (Eq. 13) of marginal instability. (But for reasons mentioned in the Appendix our result is not asymptotic in ϵ, even though the amplitude approaches zero.) The single mode truncation theory also gives reasonable agreement for the moderate μ/k_0 in the calculation (Fig. 1) at the smaller $\epsilon = 0.0344$, as indicated by the "x" points obtained from the *full* code. The circled points, on the other hand were obtained using a filtered code which suppressed all Fourier components except the (k_0, μ) and $(0, 2\mu)$ modes. This numerical truncation therefore corresponds to the analytical theory in the Appendix; and except for a small difference due to the fact that the filtered numerical calculation did not use an *explicit* $\epsilon \to 0$ approximation the circled points should lie on the analytical curve. The triangular points in Figure 1 were obtained by using the final steady data corresponding to the circular points *as initial* conditions for a temporal continuation of the calculation using the *full* code. The *slightly* different steady state obtained at $\mu/k_0 = 0.3$ might be attributed to the approximation made in the mode truncation calculation (circles). At $\mu/k_0 = 0.5$ there is no difference between the circle and the triangle, and thus the small difference between the triangular and "x" points *may* be significant and may indicate multiple steady solutions for the same (k_0, μ). We will not pursue this point, but proceed to make an extensive series of calculations for one value of ϵ with decreasing μ.

Very good agreement of the analytical theory (curve) with the result of the *full* code was obtained for $\epsilon = 0.0714$ (Fig. 2a) at $\mu/k_0 = 0.4, 0.5, 0.6$), but at $\mu/k_0 = 0.2$ the numerically computed steady state (x-point) has twice the amplitude [as measured by $|(-\overline{wT'})|^{1/2}$] of the theoretical curve. The reason for this discrepancy is clear from the presence of the thin "boundary layers" (Fig. 2b) in the mean profiles (θ, σ), since these are associated with the high m modes neglected in the theory. The highest $k > k_0$ modes, on the other hand, are negligible, as verified by a duplicate run with another filtered code with suppressed all $k > k_0$. When $\mu/k_0 = 0.1$ (Fig. 2a) a steady state was also obtained with an even larger amplitude, but this state required the use of a pure "sine-z" Fourier series, i.e., a filtered code was used to suppress the growth of all noise generated "cosine-z" components. Although this yields a consistent steady solution, with fixed horizontal nodal surfaces ($\psi = 0$), it is unstable since some of the suppressed "cosine-z" components with small m can be linearly amplified, even in the presence of the other finite amplitude components. This was convincingly verified by using the steady solution ($\mu/k_0 = 0.1$) as an initial condition for the *full* code; the evolution of the numerical noise then produced a complex non-stationary regime (not shown) without horizontal nodal surfaces. This case will now be discussed using more controlled initial conditions.

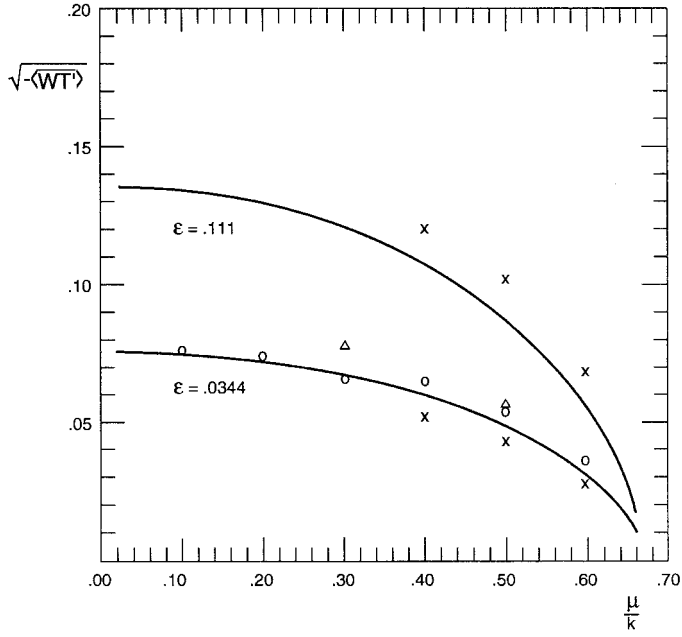

Figure 1. Steady solutions of the high Prandtl number equations at $\tau = 1/3$ for the amplitude (as given by the square root of the average convective heat flux) as a function of the fundamental Fourier wave number (μ) in the z-direction. The fundamental x wavenumber is $k_0 = (\epsilon/3)^{1/4}$. (a) $\epsilon = 0.111$ (or $R = 2.7$). The equilibrium amplitude computed by the unfiltered code was used to obtain the three "x" points, and the solid curve was obtained from the single mode truncation theory, Eq. (A7). (b) $\epsilon = 0.034$. The "x" points are from the unfiltered code; the circled points are from a filtered finite amplitude *numerical* code which closely corresponds to the single mode truncation *analytical* theory; the triangles are from a temporal continuation of the circled runs using the unfiltered code (see text).

b. Unsteady solutions for $\mu/k_0 \leq 0.1$

The previous $\epsilon = 0.0714$, $\mu/k_0 = 0.1$ run was repeated using the *full* code and the slightly different initial condition

$$T'(x, z, 0) = 0.2[0.9 \sin k_0 x \cos \mu z + 0.1 \sin (k_0 x + \mu z)], \tag{26a}$$

wherein the previous "vertical" mode is supplemented with a relatively small amplitude (0.1) "oblique" normal mode, so that the nodal surfaces ($T' = 0$) are no longer horizontal. Both modes in Eq. (26a) grow at the same rate, and both reach finite amplitude, along with their generated $m > \mu$ harmonics. The space-time complexity of the regime can be ascertained by the variation of the θ plots (Fig. 3), and by the streamlines (Fig. 4) of three adjacent horizontal wavelengths at $t = 1700$. Note the intense small scale eddies between the larger scale updrafts and downdrafts. In Figure 4 the spatially averaged convective heat

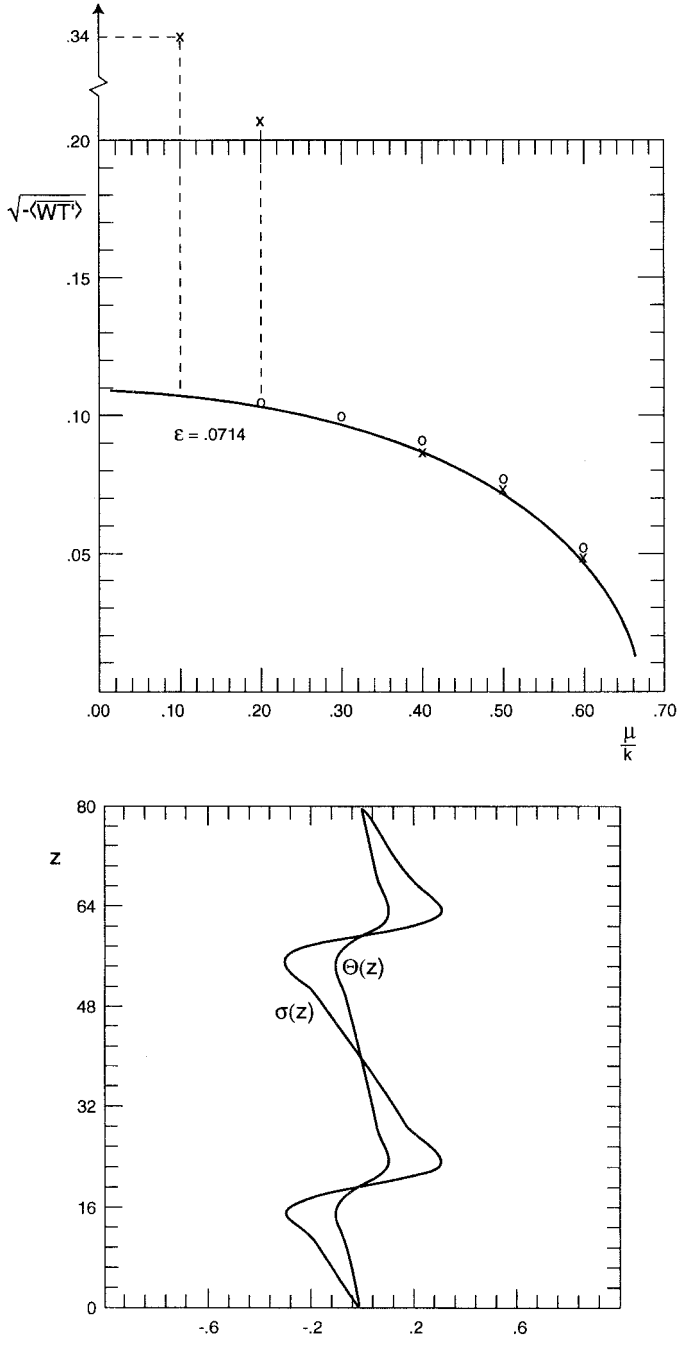

Figure 2. (a) Same as Figure 1 except $\epsilon = 0.0714$ ($R = 2.8$). Note that unfiltered runs at $\mu/k_0 = 0.2$, 0.1 give steady amplitudes very much larger than the single mode theory for the same μ/k_0. (b) Vertical profiles of the modification (θ, σ) of the horizontally averaged (temperature, salinity) profiles for $\mu/k_0 = 0.2$. Note the high $m > \mu$ harmonics associated with the large gradient regions. The total vertical distance is one fundamental vertical wavelength.

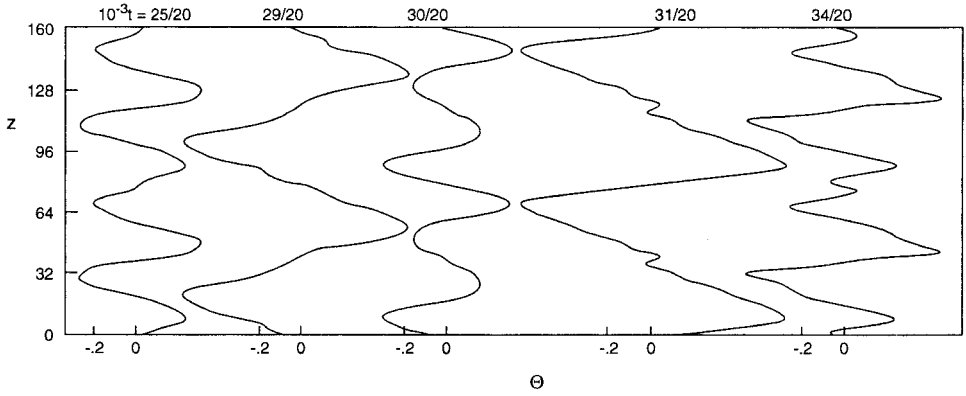

Figure 3. $\epsilon = 0.0714, \mu/k_0 = 0.1$. The mean temperature profiles $\theta(z, t)$ in one vertical wavelength at various times (t) obtained from the initial condition (26a).

flux

$$-\langle \overline{wT'} \rangle = 0.206 \tag{26b}$$

is almost twice the steady value in the constrained (sine-z series) run at $\mu/k_0 = 0.1$ in Figure 2a, but the flux oscillates in time, as will be seen.

It is important to mention that although the $2k_0$ harmonic of T' (Fig. 4) has a much smaller amplitude than the fundamental k_0 of maximum growth rate, the presence of this harmonic is crucial for limiting the time average amplitude. To demonstrate this the run initialized with Eq. (26a) was repeated using a filtered code which suppressed all $k > k_0$ (while retaining all m). After increasing to a very large value at $t = 1300$, the heat flux at $2000 < t < 5000$ settled down to a value which exceeded (26b) by a factor of thirty! An explanation of the importance of the $2k_0$ harmonic can be obtained from the power integral (21) of the asymptotic $\epsilon \to 0$ theory. If $T_{k,m}$ denotes the amplitude of the (k, m) Fourier component then the "dissipation" term $\Sigma\, k^6 T_{k,m}^2$ on the l.h.s. of (21) is clearly weighted towards $k > k_0$, and we found that for Figure 4 the contribution of the $2k_0$ harmonic to the dissipation exceeded that of the fundamental (k_0) by a factor of three; all the other ($k > 2k_0$) harmonics have negligible contribution. The $k > k_0$ harmonics are also dynamically important insofar as their complete suppression will eliminate the "triad or mode-interaction" term (e.g., term ③ in Eq. (24)). This small-scale effect provides a horizontal "eddy diffusivity' which can reduce the average buoyancy force on larger vertical scales.

To examine the effect of decreasing μ, we start with a *full* code calculation of the evolution of

$$T'(x, z, 0) = 0.2 \sin k_0 x \cos 2\mu z + 0.02 \sin k_0 x \cos \mu z, \tag{27a}$$

$$\mu = (0.05)k_0, \tag{27b}$$

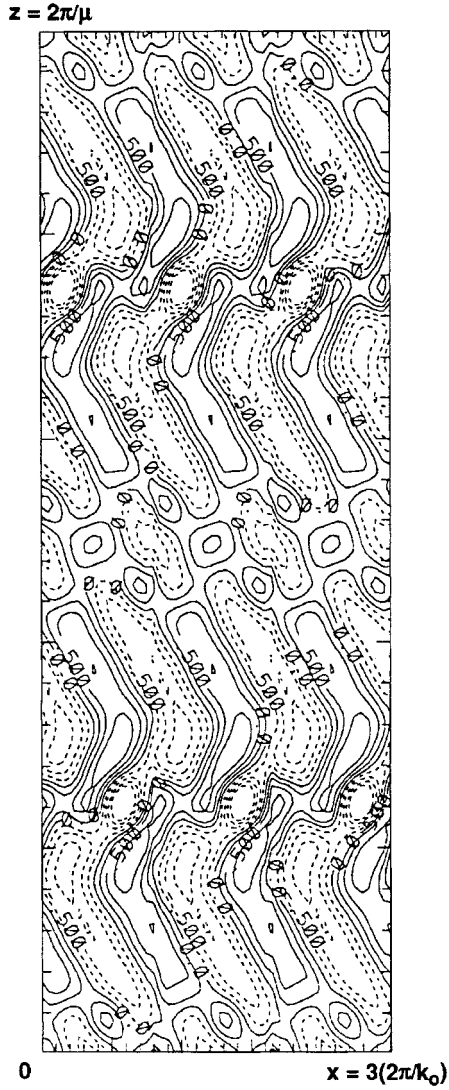

Figure 4. A plot (with no geometrical exaggeration) of the streamlines at $t = 1700$ in Figure 3 for three adjacent horizontal wavelengths and one vertical wavelength. The contour interval is 0.25. The vertically averaged heat flux is 0.21 at this time.

whose fundamental (μ) amplitude is an order of magnitude smaller than its first harmonic (2μ); this choice was made in order to proceed expeditiously toward a $\mu \to 0$ sequence in which $T_{k,m}$ decreases monotonically with m. Since $\mu \ll k_0 = (\epsilon/3)^{1/4} = (0.0714/3)^{1/4}$, the amplitudes of both normal modes in (27a) grow at nearly the same rate. Eventually $-\langle\overline{wT'}\rangle$ settles down and oscillates between two bounds prior to $t = 1450$ (not shown), at which

time both modes have increased their amplitudes by a factor of eight; the dominant harmonics (k_0, 6μ) and (k_0, 7μ) have respective amplitudes (six, four) times the fundamental (k_0, μ). The heat flux $-\langle \overline{wT}' \rangle$ at $t = 1450$ is only slightly larger than the value (26b) for the run (Fig. 4) with half the fundamental wavelength.

At $t = 1450$ (Fig. 5) we added a new and longer fundamental wavelength $\mu = (0.05/2)k_0$ with

$$T' = 0.1 \sin(k_0 x) \cos \mu z, \qquad \mu = (0.05/2)k_0.$$

The amplitude of this fundamental is smaller than that (0.162) of the $m = 0.05k_0$ mode which constituted the fundamental immediately before $t = 1450$. The number of grid points was also increased from (16, 128) to (16, 256), and then the calculation was continued to $t = 10{,}000$. The time variation of the heat flux is shown in Figure 5a, and the time average, or

$$-av\langle \overline{wT}' \rangle = 0.26 \tag{28a}$$

appears to be statistically stationary; for the *shorter* time span of the rms spatially averaged T' (Fig. 5b) we have

$$\langle \overline{(T')^2} \rangle = (1.17)^2. \tag{28b}$$

In the $\epsilon \to 0$ limit, Section 2b gives $w = \partial^2 T'/\partial x^2 (1 \pm O(\epsilon))$, and therefore

$$\lim_{\epsilon \to 0} -\frac{\langle \overline{wT}' \rangle}{\langle (\overline{T'})^2 \rangle} = \frac{\langle \overline{(\partial T'/\partial x)^2} \rangle}{\langle (\overline{T'})^2 \rangle} \cong k_0^2 = \left| \frac{\epsilon}{3} \right|^{1/2} = 0.15, \tag{28c}$$

a result which is 15% smaller than the ratio of (28a) to (28b), but within the estimated error bounds $1 \pm O(\epsilon)$ of the asymptotic theory.

Figure 6 gives the spectrum E_m on the thermal variance at various times for $m \geq \mu$, where

$$\sum_{N=0}^{\infty} E_m(t) = \langle (\overline{T'})^2 \rangle, \qquad N = \frac{m}{\mu}.$$

The spectral peak in the time average (Fig. 7) occurring at $m = 15\mu = (15/40)k_0$ is almost three times the finger wavelength. Although the $m = 0$ component, which is numerically generated and calculated in the Fourier series code, is not shown, its value at $t = 8500$ is only ⅓ the value of E_μ (i.e., for $N = 1$).

The $\psi(x, z, 10^4)$ plot (Fig. 8), of three adjacent horizontal wavelengths, reveals both large scale coherence, and the disorder on the smaller ($m = k_0$) vertical scale. Thus some ψ lines can be traced on a diagonal path over an infinite distance, while some ψ lines are

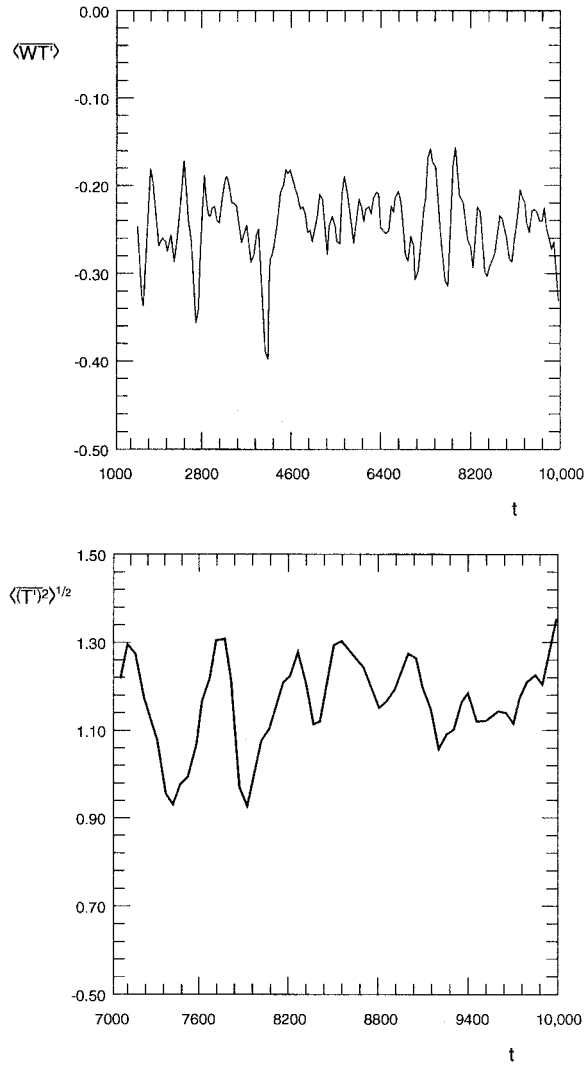

Figure 5. (a) The heat flux as a function of time for $\epsilon = 0.0714$. The initial condition Eq. (27) consisted of a relatively small amplitude fundamental ($\mu = 0.05k_0$) mode and a first harmonic ($m = 2\mu$). At the end of the initial phase ($0 < t < 1450$) a longer fundamental wavelength ($\mu = 0.05/2k_0$) was introduced (see text) and then the calculation was continued to $t = 10{,}000$. (b) The rms horizontal temperature fluctuation as a function of t.

closed curves, and others are inclined quasi-laminar columns. The great irregularity of the horizontally averaged temperaure is revealed in Figure 9.

The accuracy and sensitivity of the foregoing calculation is indicated by the three curves in Figure 10. The dashed one starting at $t = 7050$ (and reproducing Fig. 5a) used a time step $\Delta t = 0.05$; the solid curve was initiated with the same data set, but it had a time step of

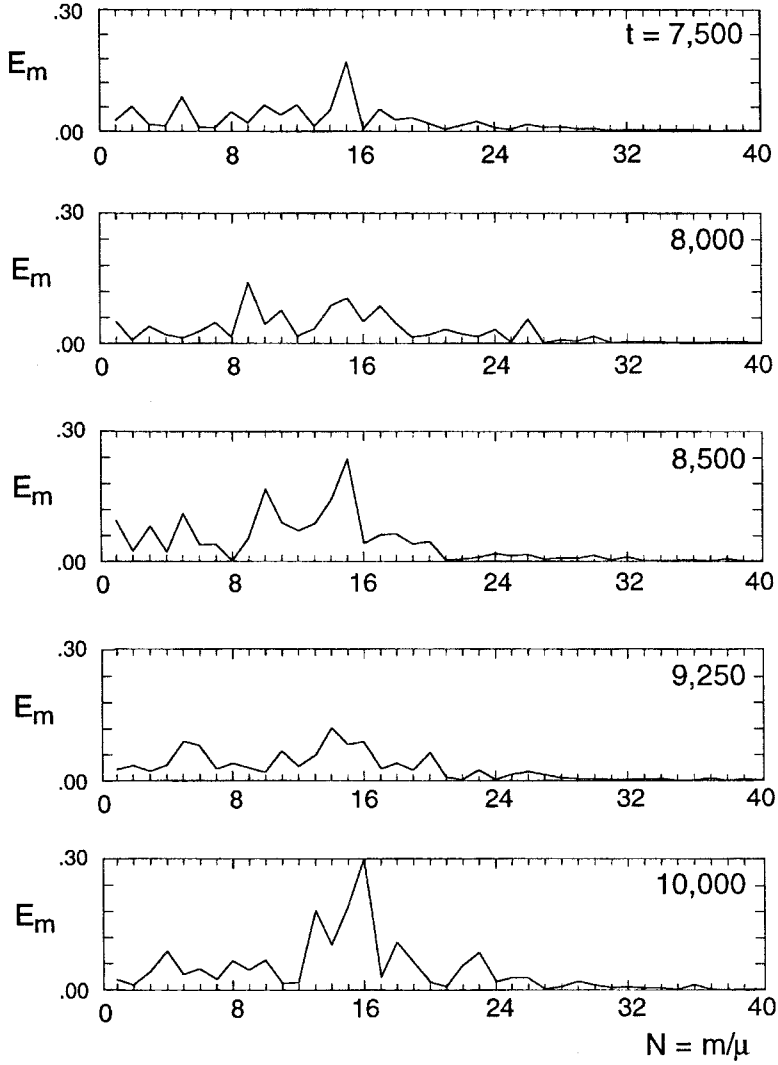

Figure 6. Vertical spectrum of $(T')^2$ for Figure 5 at various times. $E_m(t)$ is the total Fourier energy in mode m. The sum over all integral values of the abscissa $N = m/\mu = m/0.025k_0$ gives the spatially averaged value of $(T')^2$. Not all the very large m computed with the spectral code are shown. The $m = 0$ value is also not shown here, but its value at $t = 8500$ is only ⅓ the value of E_m at $N = 1$ ($m = \mu$).

0.05/2. These two curves are barely distinguishable up to $t = 8500$. The dash-dot curve was obtained by making a very small change in initial conditions (i.e., the data at $t = 7150$), viz., by deleting (only) the extremely small $k \geq 3k_0$ Fourier components at this time; then the calculation was continued with *all* subsequently generated k allowed. Although the

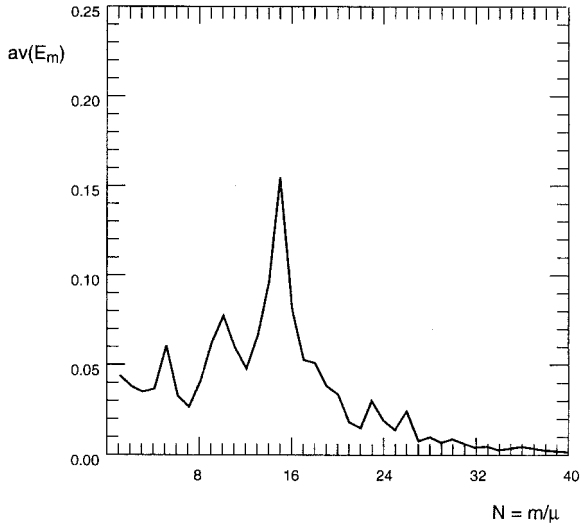

Figure 7. The time averaged E_m in Figure 6. The peak wavelength is approximately three times the (finger) wavelength of k_0. Although the amplitude at $m \equiv 0$ is not shown, it is finite but much less than at $N = 1$ ($m = \mu$).

resulting curve is not distinguishable from the other two up to $t = 7500$, there is a significant difference from that time to the end ($t = 8000$). Thus the detailed time dependent history is extremely sensitive to small perturbations, but this and other (short) calculations in which the $k \geq 3k_0$ modes were *permanently* suppressed (by the code) indicate that the time average heat flux is rather insensitive to such perturbations.

4. Subharmonic instability

In all preceding calculations the fundamental Fourier component k_0 is the wavenumber (13) which grows the fastest on the undisturbed field, whereas all harmonics ($2k_0$, $3k_0$, . . .) are damped. The subharmonics ($k_0/2$, $k_0/3$), however, can grow, and we now consider what happens when such a disturbance of relatively small amplitude is present.

The final data ($t = 10^4$) for the run in Figure 5a was therefore augmented by adding the subharmonic ($k_0/2$) perturbation

$$T' = 0.02 \sin (k_0 x/2 + \mu z), \qquad \mu = k_0/40 \tag{29}$$

on the chaotic field. The total $T'(x, z, 10^4)$ was interpolated on a 16×256 grid so that the cutoff $k = 4k_0$ was half its previous value (we have reason to believe that the $k > 4k_0$ waves are unimportant). The continuation of the calculation in Figure 11 shows that although the maximum disturbance energy (Fig. 11b) shifts from $m = 15$ (Fig. 7) to much *longer* wavelengths, there is a precipitous drop of both the heat flux and the rms temperature;

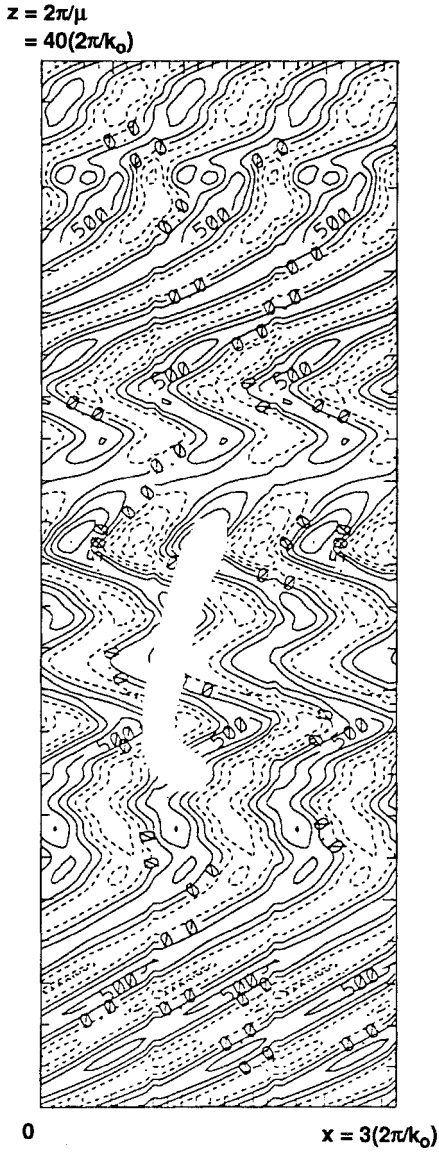

Figure 8. The streamlines in three adjacent horizontal wavelengths ($k_0 = 0.40$) and one fundamental vertical wavelength ($\mu = 0.025k_0$). The plot in the vertical should be stretched by a factor of approximately five to remove the horizontal exaggeration. The contour interval is 0.25.

stable averages are reached with values considerably *smaller* than occur in the absence of the subharmonic. This calculation shows that the average properties remain bounded even as the domain size increases. It also establishes the instability of the solution obtained in the previous section, and indicates the importance of long ($k < k_0$) waves. Apparently these

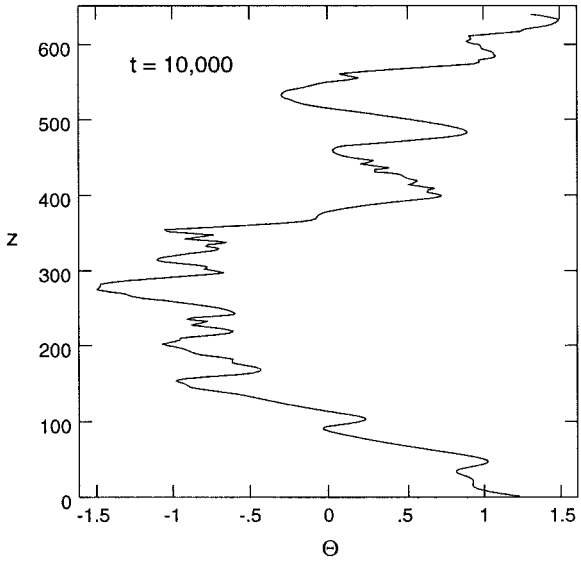

Figure 9. The horizontally averaged temperature disturbance (θ) over one vertical wavelength, at one particular time. This fundamental vertical wavelength is four times that in Figure 3.

reduce the heat transport because they can grow on the mean field, thereby contributing more to the triad or mode interaction term ($\mathbf{V} \cdot \nabla T'$) than does the very small amplitude $2k_0$ mode. As previously suggested, the mode interaction term produces a lateral eddy heat flux convergence which can diminish the buoyancy of the vertical fingers.

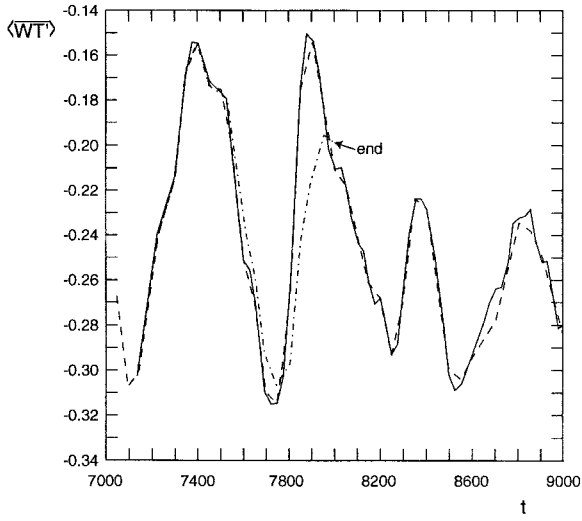

Figure 10. Accuracy and sensitivity test of Figure 5 (dashed curve). The solid curve is a rerun using the same initial ($t = 7150$) conditions but half the time step. The dashed-dot curve was obtained by using slightly altered initial conditions (see text).

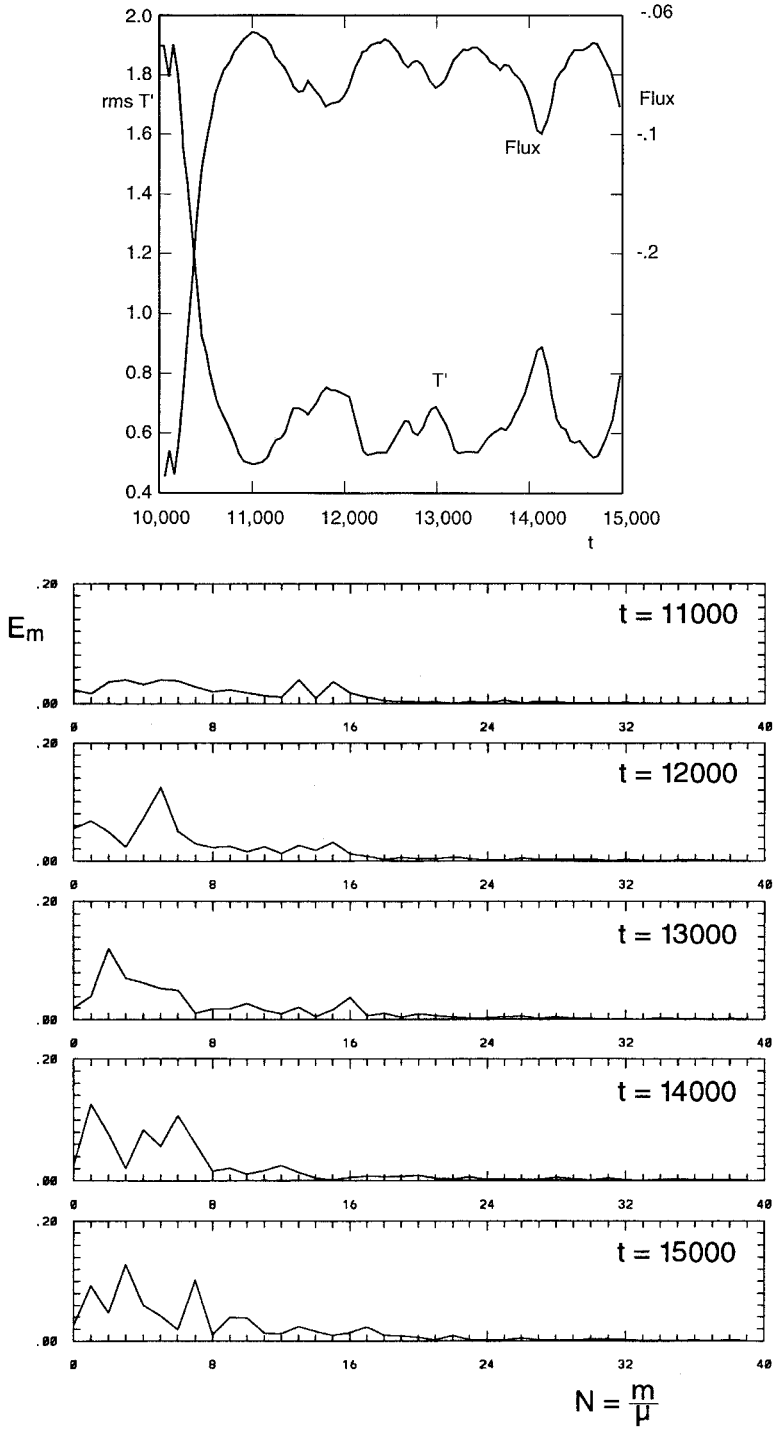

Figure 11. The effect of adding a small amplitude subharmonic ($k_0/2$) perturbation (29) to the state of Figure 5a at $t = 10^4$. (a) Both the rms temperature fluctuation and heat flux drop precipitously to new temporal averages. (b) The total energy in mode m shifts from a previous maximum at $N = 15$ to much longer wavelengths.

a. **a.**

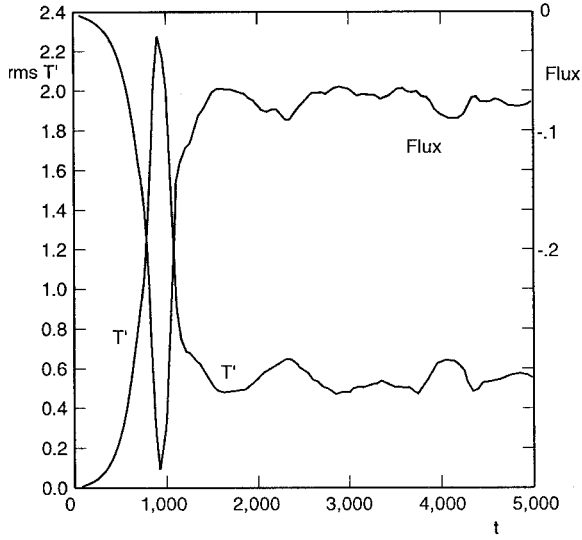

Figure 12. A run starting from rest with a perturbation (31) containing a fundamental horizontal wavenumber which is ⅓ of the fastest growing one (k_0). (a) The final average heat flux and rms temperature perturbation are slightly less than their averages in Figure 11a. (b) The T' isopleths at $t = 5 \times 10^3$ illustrates the chaotic character of the field. The grid size is 32×256. The contour interval is 0.3. (c) The horizontally averaged temperature field at $t = 4 \times 10^3$ in a fundamental x and z wavelength. This illustrates the variability of the average heat flux at each z. (d) The total energy in wave number k where $k_m = k_0/3$ is the smallest subharmonic wavenumber. The numbers on the curve are the values of $t \times 10^{-3}$. At $t = 5000$ there is as much energy in the long waves ($k/k_m < 3$) as in the short waves. Both are essential for the statistically state ($t > 1500$ in Fig. 12a).

Similar results were obtained for a run initialized from *rest* with a subharmonic, so that the total temperature perturbation was

$$T'(x, z, 0) = 0.2 \sin k_0 x \cos 2\mu z + 0.02 \sin k_0 x \cos \mu z + 0.02 \sin k_0 x/2 \cos 2\mu z, \qquad \mu = k_0/40. \tag{30}$$

In this case (not shown) the average energy at $t = 10^4$ had a pronounced maximum at $N = 1$ or $m = \mu$, i.e., at the *longest wavelength allowed* in the calculation. We note that this fact, like the similar situation in the Appendix where the longest wave contains all the energy, poses no problem for our "unbounded" model, which only requires that the energy be bounded as the maximum allowed wavelength increases, and we have shown that this does occur. Of course, in a real (bounded) experiment like the one mentioned in the introduction, the domain is of finite vertical extent, and *boundary layers* are required at the top and bottom. Such regions may be allowed for in our model, and it is reasonable to assume they will not affect the amplitude in the deep interior.

Figure 12 shows the result of another run in which the minimum wavenumber was

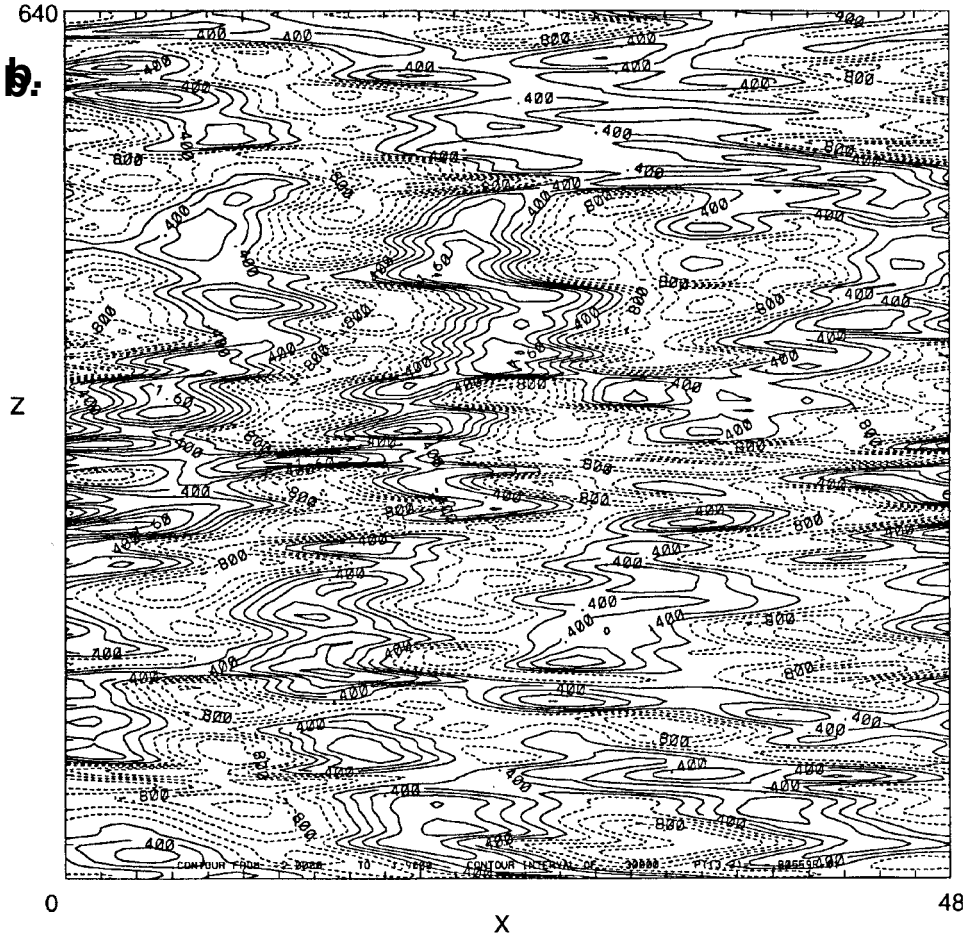

Figure 12. (Continued)

decreased from $k_0/2$ to $k_0/3$, using the initial perturbation:

$$T'(x, z, 0) = 0.2(\sin k_0 x)\cos 2\mu z + 0.02(\sin k_0 x)\cos \mu z + 0.02(\sin k_0 x/3)\cos 2\mu z, \qquad \mu = k_0/40. \tag{31}$$

The resulting heat flux and rms temperature (Fig. 12a) now levels off at values *slightly less* than occurred previously, and most of the energy is again in the longest permitted wave. The chaotic character of the detailed (x, z, t) field in three pairs of fingers is revealed by Figure 12b (for T') and by Figure 12c for the mean temperature disturbance (θ). Figure 12d indicates that the two subharmonics have as much energy as the fastest growing horizontal wavelength.

c.

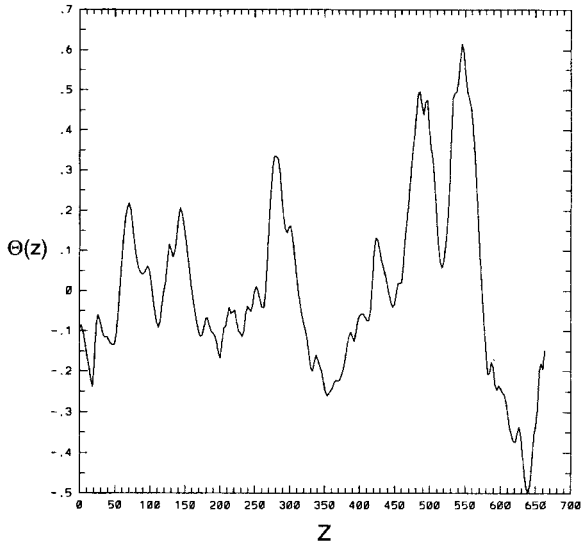

d.

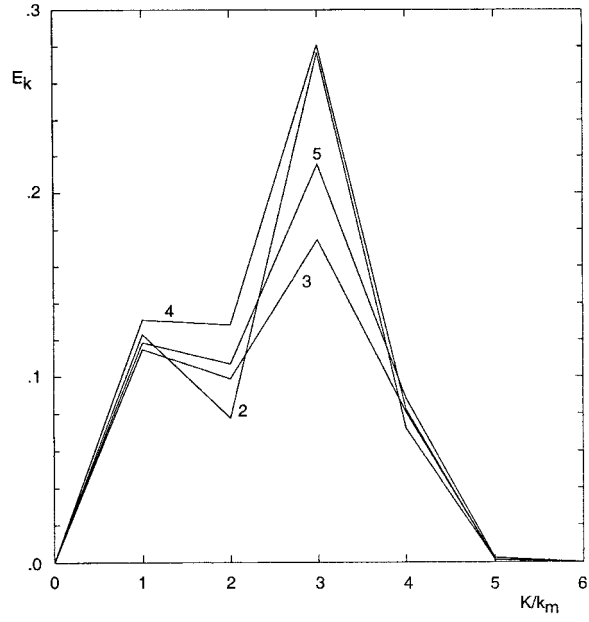

Figure 12. (Continued)

5. Extension to smaller *R*

Since the experimentally realized values of *R* are much smaller than the previous one, we now proceed to decrease *R*. But when *R* in the subharmonic run of Section 4 was decreased below 2.65 a numerical instability led to a crash, the cause of which is first investigated.

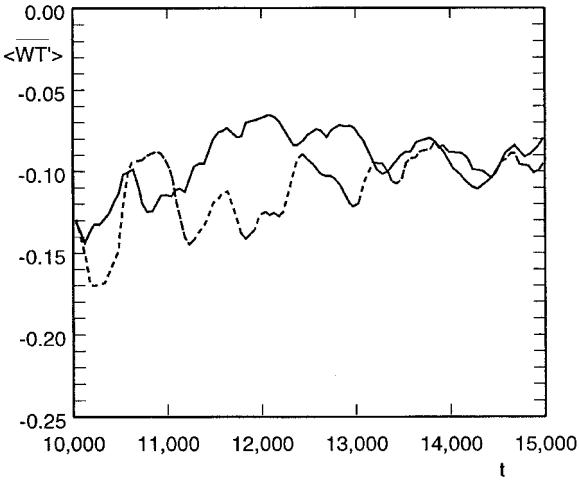

Figure 13. The heat flux as a function of time for $\epsilon = 0.0714$. The dotted line presents the continuation of the calculations in Figure 11a) (using the same code with 256 harmonics). The solid line presents the calculations also initiated by the final ($t = 15{,}000$) data of the run in Figure 11a but continued with the use of a dealiased code (using 128 harmonics). While the details of the variation of the heat flux in time are significantly different in these two cases, the statistical averages suggested by the codes are fairly consistent.

a. Accuracy of the spectral approximation of spatial derivatives

The crash was not alleviated by decreasing the time step, which indicated that the source of such an instability was not related to the well-known Courant-Friedrichs-Lewy (CFL) limitation on the Δt in the explicit schemes. The numerical instability was attributed to the so-called aliasing effect, which is associated with the discrete Fourier images (instead of the exact ones) used in the code. Aliasing results in the artificial flux of energy to the longer vertical wavelengths, and their subsequent linear amplification over time might lead to the crash. In contrast to CFL instability, aliasing obviously becomes more significant with increasing spatial separation of the grid-points, and therefore most of the calculations presented below employed a dealiasing "zero-padding" routine (Canuto *et al.,* 1987) which is effective for the integration of the differential equations with quadratic nonlinearities; dealiasing in z (only) proved sufficient to stabilize the code. In that which follows we will examine how the behavior of the salt fingers depends on the spatial resolution in both aliased and dealiased codes, and this will indirectly indicate the range of scales of the eddies that affect the statistically averaged characteristics of the flow.

The final data for the run in Figure 11a,b have been used to initiate a dealiased code, with 128 nontrivial Fourier harmonics (compared to 256 used previously). The calculations, extended to $t = 20{,}000$, are presented in Figure 13, which presents heat flux plotted as a function of time for calculations made with a dealiased code (solid line) and with the previously employed aliased one (dashed line). We can see that while the detailed behavior

Table 1. The heat flux averaged over the period of time $15000 < t < 17500$ as a function of resolution in the aliased and dealiased codes; λ_{min} denotes the shortest (in z) wavelength properly resolved by the code. For comparison, the *horizontal* wavelength for the fastest growing mode is 16 of the above units.

	$\lambda_{min} = 40$	$\lambda_{min} = 20$	$\lambda_{min} = 10$	$\lambda_{min} = 5$
dealiased	−0.84	−0.20	−0.12	−0.11
aliased	unstable	unstable	unstable	−0.12

is different in the two cases, the statistically averaged values of heat flux, for the two codes tend to approximately the same value. Similar behaviors were obtained for the temperature variance (not shown).

The calculation in Figure 13 has also been made with lesser resolutions of 64, and then 32 nontrivial harmonics; and with the better resolution of 256 harmonics. The results presented in Table 1 demonstrate that the eddies with a vertical scale comparable to the horizontal wavelength of the fastest growing normal mode can substantially contribute to the integral properties of the salt fingers. Note that the attempts to decrease the resolution of the aliased calculations below the level provided by 256 harmonics ($\lambda_{min} = 5$) resulted in the numerical instability of the aliased code. This discussion indicates that some of our previous runs are "marginally resolved" numerically; the properly resolved runs yield consistent results for both the aliased and dealiased calculations, while under-resolved runs resulted in the numerical destabilization of the former and in the inaccurate results of the latter code. From Table 1 we can see that it is absolutely necessary to resolve (we used four grid points) vertical scales which are at least $\lambda_{min} = 10$, a vertical wavelength which is comparable with the horizontal wavelength of the salt fingers (16 units). This might seem somewhat hard to understand, since the amplitude of the high (in z) modes is quite small as was indicated in the previous sections, and therefore we give another, even more dramatic, example of the numerical effects that might occur because of neglecting the (small amplitude) high z modes.

We reproduced our earlier calculation in Figure 5a, which was made without introducing the subharmonics, using a dealiased code with a lesser resolution of 64 nontrivial modes (for $t < 1450$) [instead of 128 modes employed in the old (aliased) calculation], and for $t > 1450$ we used 128 modes [instead of the 256 modes used before]. All the other parameters and procedures, such as the use of Eq. (27a) to initiate the run, have not been changed. The time variation of the heat flux of this (under-resolved) dealiased calculation is shown in Figure 14, and the spectrum E_m of the thermal variance at $t = 10{,}000$ is presented in Figure 15. The fundamental differences between this and the old calculation (see Fig. 5a) become quite apparent from both of the figures (cf. Figs. 14, 15) presented. The absence of the oscillations of the heat flux at the large times ($t > 5000$) indicates that it is the small-scale eddies that are responsible for the temporal variability of the integral properties. Note also that (after a period of adjustment) heat flux settles down to a value (−0.12) which is less than half of the statistical average suggested by our old calculation in Figure

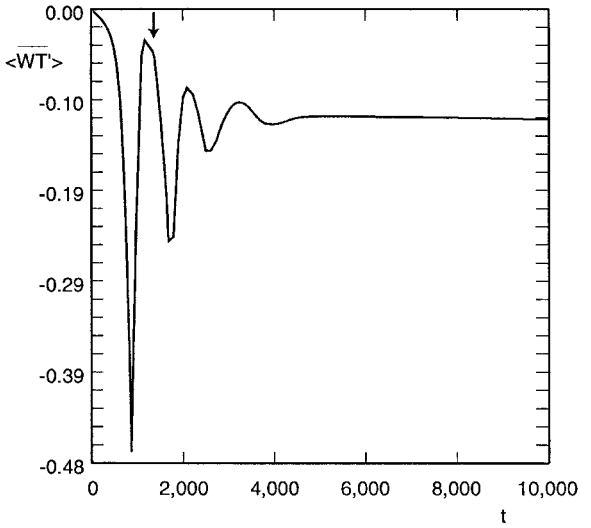

Figure 14. The under-resolved dealiased calculation initiated exactly as the run in Figure 5a. The shortest z-wavelength resolved by the code is 10.0 (compared to the 5.0 for the run in Fig. 5a). The decrease in the resolution resulted in the complete disappearance of the chaotic oscillations of the heat flux at the late stage of the experiment. The arrow is at $t = 1450$ (see text).

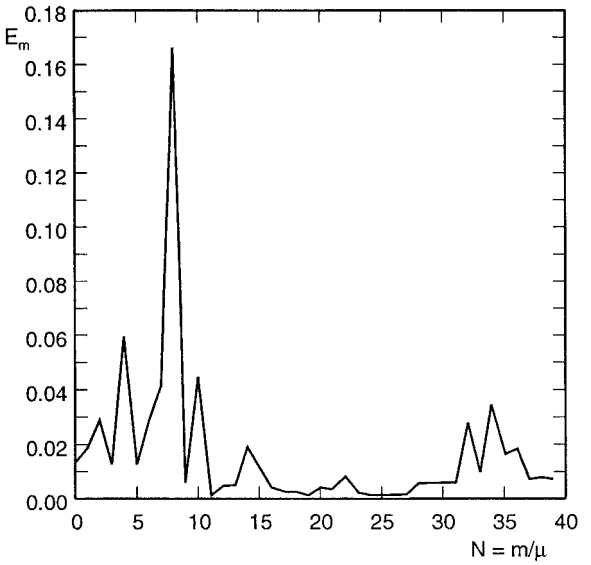

Figure 15. Vertical spectrum of $\langle \overline{T'^2} \rangle$ at $t = 10{,}000$ in the under-resolved run. Failure of the code to resolve the small-scale eddies resulted in the significant modifications of the spectrum (compare to Figs. 6, 7).

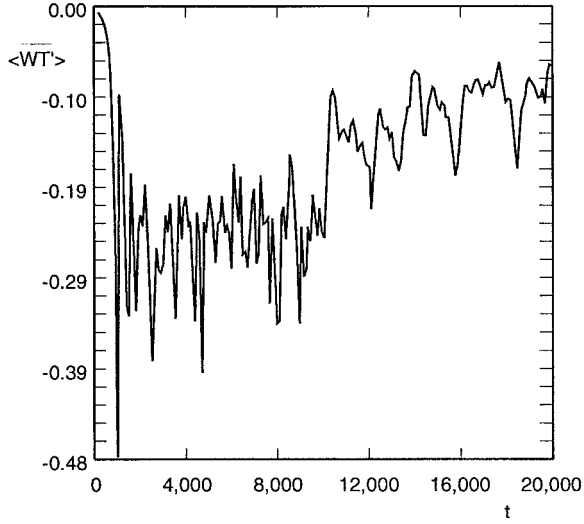

Figure 16. The heat flux as a function of time for $\epsilon = 0.0714$ ($R = 2.8$). In this calculation a "zero padding" method was employed to remove the aliasing error associated with the z-modes. The initial conditions (32) consisted of a relatively small amplitude fundamental ($\mu = 0.05k_0$) mode and a second harmonic ($m = 2\mu$). At the end of the initial phase ($0 < t < 10{,}000$) the size of the computational domain in x was doubled, and the (small amplitude) subharmonic $k = 0.5k_0$ was included, and the calculation was extended to $t > 10{,}000$. Note that the time averages of the heat flux obtained are quite consistent with those suggested by our previous experiments in Figure 5a, 11a for both phases of the experiment.

5a. However, when the proper resolution is used in the dealiased code [see Fig. 16 at $t \leq 10{,}000$] the result is consistent with that in Figure 5a. The spectrum E_m (see Fig. 15) of the under-resolved run is characterized by the two local maxima, the second of which occurs in the vicinity of the $N = 32$ harmonic. Thus the distribution of thermal variance E_m is also quite different from the spectrum of the corresponding (properly resolved) old run in Figure 7. The pattern of spectrum as presented in Figure 15 proved to be fairly persistent and did not change essentially in the late stage of the experiment ($2{,}000 < t < 10{,}000$), even when the described experiment was modified by deleting (numerically) at $t = 2{,}000$ all of the $N > 25$ z-modes; the local maximum in the vicinity of $N = 32$ reappears at the later times.

This discussion demonstrates the importance of the small-scale eddies for the dynamics of long fingers at finite ϵ. The similary theory ($\epsilon \to 0$) of Section 2, pertaining to vertical scales larger than the fingers, should therefore not be extrapolated to the finite ϵ calculations herein.

In order to examine the accuracy of the time-stepping scheme (beyond that which was done in Section 3b where Δt was decreased by a factor of two) we have used an alternative method of integration, characterized by the use of the so-called integrating factors technique (Canuto *et al.,* 1987). This method can be conveniently used for the systems of

differential equations with nonlinear advective and linear diffusive terms, such as was done, for example, in the aforementioned work by Whitefield *et al.* (1989). An exceptionally good agreement between the results provided by this method and the one described and employed previously allowed us to conclude that the accuracy of the time-stepping is more than sufficient. However, the use of the integrating factors did not allow us to relax the limitation on the time step, and for that reason all of the following calculations have been made with the "old" straightforward fourth-order Runge-Kutta integrating scheme.

b. Calculations for the low R

All of the lower R runs were made using the dealiased code, and since some of our calculations (not presented) indicated that the statistically averaged characteristics of the system do not change as μ/k_0 is decreased below 0.05, the following calculations are restricted to $\mu/k_0 = 0.05$. To initiate the run of the dealiased code we used

$$T'(x, z, 0) = 0.2[0.9 \sin k_0 x \cos 2\mu z + 0.1 \sin (k_0 x + \mu z)], \tag{32}$$

where k_0 is the x-wavenumber of the fastest growing mode, μ is the fundamental wavenumber in z, and 128 nontrivial harmonics in z were used with 16 in x. In all the calculations $\tau = \frac{1}{3}$, and we again start with $R = 2.80$, and $\Delta t = 0.1$.

To expedite the calculations over the range of t and R the following procedure was adopted. For $t < 10{,}000$ the calculation in Figure 16 contains no subharmonic. At $t = 10{,}000$ we increased the size of the computational domain (in x), so that the fundamental wavelength in x became twice that of the fastest growing mode, and this allowed us to introduce (at $t = 10{,}000$) the small amplitude subharmonic perturbation

$$S' = T' = 0.02 \sin (k_0 x/2 + \mu z)$$

to the (T, S) field. The ratio of the computational domain was kept 1:10 in all calculations for $t > 10{,}000$. As can be seen from Figure 16, the average value of the heat flux is quite consistent with our earlier estimates (see Sections 3 and 4) in both regimes (i.e., with and without the subharmonic).

At $t = 20{,}000$ the value of R was decreased to $R = 1/0.36 = 2.78$. Although the values of (T, S) at the grid-points were not changed, the spatial separation between the grid-points was decreased to reflect the small modification of the x-wavelength of the fastest growing normal mode (which occurs due to the decrease of R). The calculations were then carried on for an additional 2,500 time units, which was sufficient to approximate the statistically steady values of the heat flux and the temperature variation for that R. Subsequently R was decreased several times in a similar manner, and the integral characteristics were computed, as, summarized in Table 2. As the separation of the grid points was decreased the time step was decreased.

The detailed time variation of the heat flux and flux ratio shown in Figure 17, reveals both the dependence of the statistical averages on the value of R, and the presence of temporal oscillations of the spatial integrals. Other features of the (T, S) field observed in

Table 2. Statistically steady values of the heat flux and of the thermal variance as a function of R.

Period of time	$1/R$	$-\mathrm{av}\langle\overline{WT}'\rangle$	$\mathrm{av}\langle\overline{T'^2}\rangle$
20,000–22,500	0.36	0.13	0.80
22,500–25,000	0.37	0.27	1.49
25,000–27,500	0.38	0.55	2.69
27,500–32,500	0.39	0.87	4.01
32,500–37,500	0.40	1.84	7.96
37,500–42,500	0.41	2.78	11.46
42,500–50,000	0.42	3.77	15.89
50,000–52,500	0.43	5.48	22.11
52,500–57,500	0.44	6.96	25.66
57,500–60,000	0.45	7.41	28.45
60,000–62,500	0.46	9.22	34.71
62,500–65,000	0.47	10.9	38.8
65,000–67,500	0.49	14.9	50.7
67,500–70,000	0.52	21.8	74.3
70,000–72,500	0.55	29.8	92.8
72,500–75,000	0.60	43.5	130.8
75,000–76,250	0.63	51.9	146.0

the $\epsilon = 0.0714$ calculations (see Section 4), such as the large-scale coherence and the disorder on the smaller scales, also occur at low R as can be seen (Fig. 18) from the isopleths of the temperature $T(x, y, 60{,}000)$ for $\epsilon = 0.35$.

The distribution of the thermal variance in the vertical harmonics is presented in Figure 19 for $\epsilon = 0.35$ ($t = 60{,}000$), and is qualitatively similar to the E_m in Figure 11b for $R = 2.8$ ($\epsilon = 0.07$). The spectra of the energy E_k in the horizontal wavenumber k (not shown) has the maximum of energy shifting between the fundamental and the fastest growing modes. It is suggested that the even longer horizontal waves might become important as ϵ increases, but we will not pursue this point here; instead the heat flux and thermal variance as a function of ϵ is discussed.

Let us tentatively assume simple power laws for the heat flux and the temperature variance of the form

$$-\mathrm{av}\langle\overline{WT}'\rangle = A\epsilon^{\alpha}, \qquad \mathrm{av}\langle\overline{T'^2}\rangle = B\epsilon^{\beta}, \tag{33}$$

or

$$\ln\left(-\mathrm{av}\langle\overline{WT}'\rangle\right) = \alpha\ln(\epsilon) + \ln(A), \qquad \ln\left(\mathrm{av}\langle\overline{T'^2}\rangle\right) = \beta\ln(\epsilon) + \ln(B). \tag{34}$$

These are plotted (Figs. 20, 21) from the data of Table 2 as a function of $\ln(\epsilon)$, and the nearly straight line curves confirm the (assumed) relationship (33). The slope and intercepts of the lines in Figure 20, 21 provide a good estimate of the parameters in (34):

$$\alpha \approx 2.5, \qquad \beta \approx 2.1, \qquad A \approx 70, \qquad \text{and } B \approx 188.$$

It is obviously unjustified to extrapolate the logarithmic curves in Figures 20–21 to

$R \to 1$, where a much enhanced convective regime is expected because the overall density stratification is near neutral.

If these power laws were extrapolated to $\epsilon \ll 0.07$ they would imply heat fluxes very much less than the similarity law (Section 2) for long thin fingers, but such extrapolation is also empirically unjustified.

6. Conclusions and suggestions

We have discussed the behavior of salt fingers in an unbounded fluid with high Prandtl number and with given uniform "overall" average vertical gradients ($\overline{T}_z$ and $\overline{S}_z$), concentrating on the nearly marginally unstable initial state with $\tau = O(1)$, $R = O(1)$, and small finite ϵ. An important qualitative question is whether the fluxes for the vertically unbounded model calculation would be bounded when the fundamental vertical wavelength $2\pi/\mu$ becomes infinite, and this was answered affirmatively.

When μ^{-1} is taken to be only a small multiple of the horizontal wavelength (k_0^{-1}) of maximum growth rate, the normal mode in the numerical calculation evolves to a steady finite amplitude by modifying the horizontally averaged $T - S$ gradients on the scale of this mode; as is satisfactorily explained by a single mode truncation theory. But even for very small Reynolds number this theory fails qualitatively as μ^{-1} is increased, since many $m > \mu$ harmonics can grow; moreover, all of these modes contribute to amplitude equilibration via classical *triad* interaction effects.

The spatially averaged (nondimensional) convective heat flux $Nu \equiv -\langle \overline{wT}' \rangle$ and the rms horizontal temperature fluctuation $\tilde{T}' = \langle (\overline{T}')^2 \rangle^{1/2}$ exhibit large variations on a long time scale, and although the detailed variation is extremely sensitive to small changes in initial values the long time numerical integration of the high Prandtl number equations for $\tau = \frac{1}{3}$ and a small $\epsilon = 0.0714$ yields (convincingly) statistically steady average values. However, this solution (for k_0) was shown to be subharmonically unstable, with resulting average Nusselt number and rms temperature fluctuation (Fig. 12a) given respectively by $N = 0.08$, $\tilde{T}' = 0.55$. These subharmonic instabilities are different from those discussed by Holyer (1984), wherein the subharmonic energy comes from the equilibrium finger field rather than from the $\overline{S}_z$ field in our model.

The asymptotic ($\epsilon \to 0$) equations of Section 2 are qualitatively useful in indicating the importance of *many* long vertical wave numbers (m) and their (triad) interaction no matter how small ϵ is. These equations are limited, however, because they are not uniformly valid (viz., over long time and large m); they do not, therefore, describe the evolution of the finite $\epsilon > 0.07$ calculations made herein. The question is open, however, as to whether they describe the solution of the high Prandtl number equations for $\epsilon \ll 0.07$, since the numerical calculations cannot easily attain the asymptotic limit because of the low growth rate.

For larger ϵ or $1.6 < R < 2.7$ the Nusselt number and thermal variance are given in Table 2, and Figures 20, 21; the variation of the flux ratio with R is given in Figure 17b. An

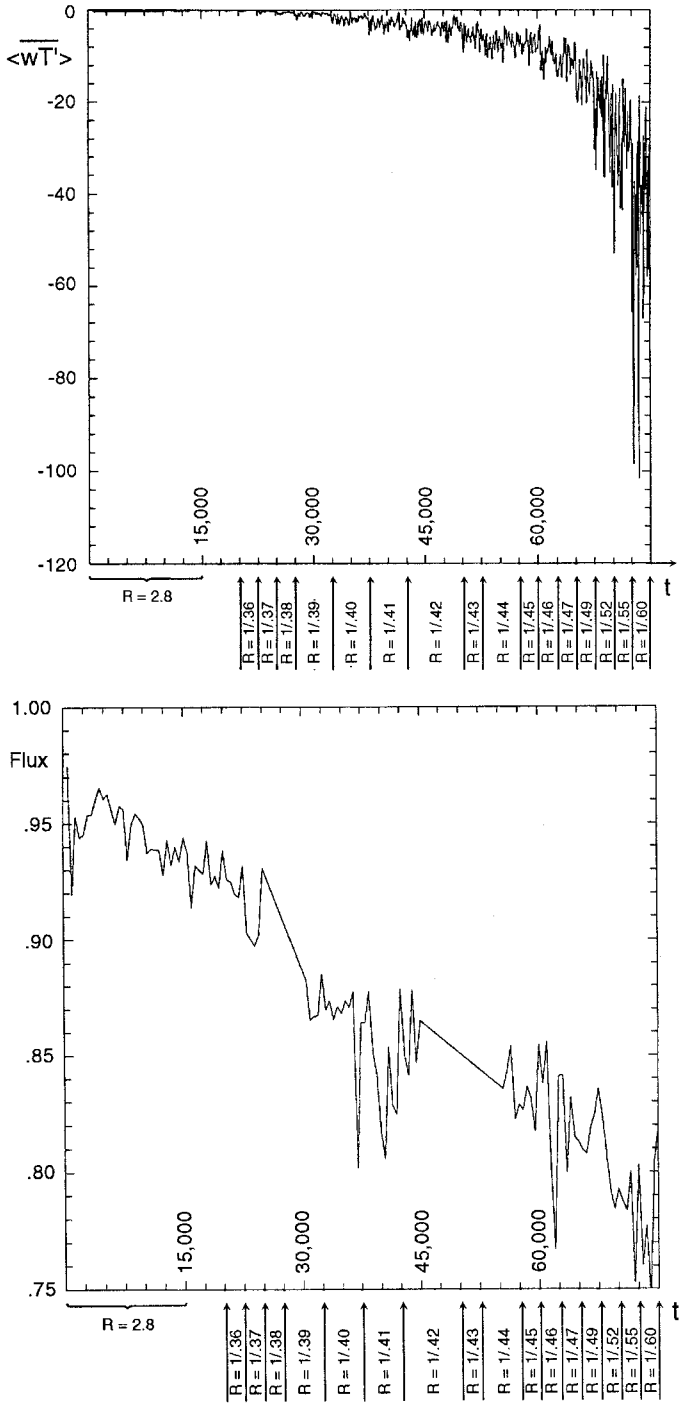
0
-20
-40
-60
-80
-100
-120
<wT'>
15,000
30,000
45,000
60,000
t
R = 2.8
R = 1/.36
R = 1/.37
R = 1/.38
R = 1/.39
R = 1/.40
R = 1/.41
R = 1/.42
R = 1/.43
R = 1/.44
R = 1/.45
R = 1/.46
R = 1/.47
R = 1/.49
R = 1/.52
R = 1/.55
R = 1/.60
1.00
Flux
.95
.90
.85
.80
.75
15,000
30,000
45,000
60,000
t
R = 2.8
R = 1/.36
R = 1/.37
R = 1/.38
R = 1/.39
R = 1/.40
R = 1/.41
R = 1/.42
R = 1/.43
R = 1/.44
R = 1/.45
R = 1/.46
R = 1/.47
R = 1/.49
R = 1/.52
R = 1/.55
R = 1/.60

Figure 17

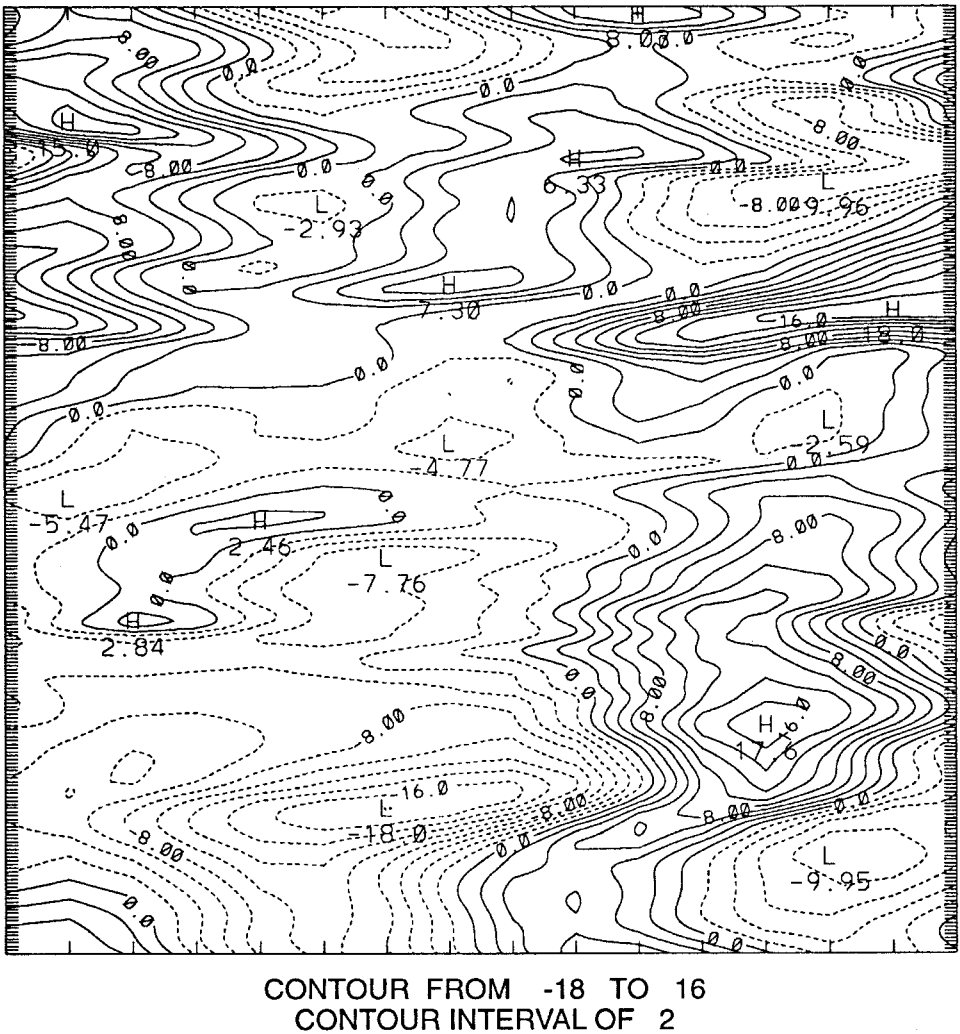

Figure 18. The isopleths of the total temperature T(x, z, 60,000) for the run in Figure 17 at e = 0.35. The horizontal scale is geometrically exaggerated by the factor of 10. Although the structure of the temperature field is similar to what was observed at the lower e (see Fig. 8), the amplitude is much larger.

Figure 17. Calculation in Figure 16 was extended in time as R was decreased several times as indicated in Table 2. (a) The evolution in time is characterized by the fast chaotic oscillations of the heat flux. However, the statistically averaged value of the heat flux (for each R) is extremely sensitive to the values of R employed. (b) The flux ratio $\gamma = \overline{\text{heat flux}}$ as a function of time for the run in Figure 17a. γ significantly decreases as we decrease R. The rough "order of magnitude" estimate suggests that $(1 - \gamma)$ is proportional to e, which is consistent with the empirical power laws obtained later in Figures 20–21. Note also significant oscillations of the flux ratio in time. There is no available data for the periods $25{,}000 < \tau < 30{,}500$ and $45{,}000 < \tau < 55{,}500$; otherwise calculations of the flux ratio have been performed each 500 units.

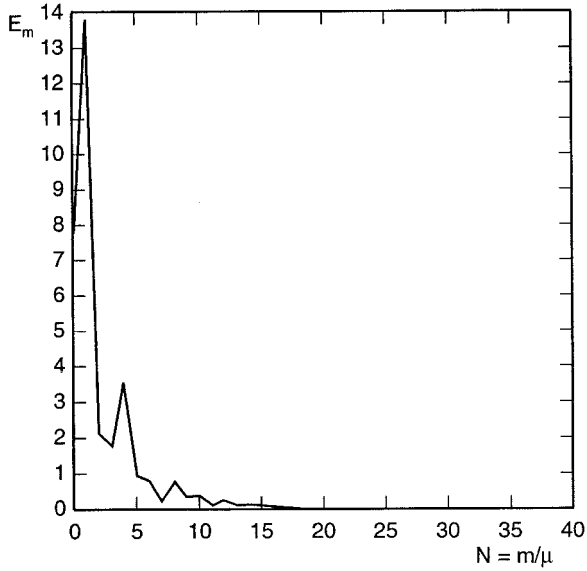

Figure 19. Vertical spectrum of $(T')^2$ for $t = 60{,}000$ (see Fig. 18). This spectrum looks fairly similar to the distribution of energy which was observed in the subharmonic calculations for the lower ϵ (Fig. 11b), except for the tendency of the energy spectrum to shift to the longer wavelengths when ϵ is increased.

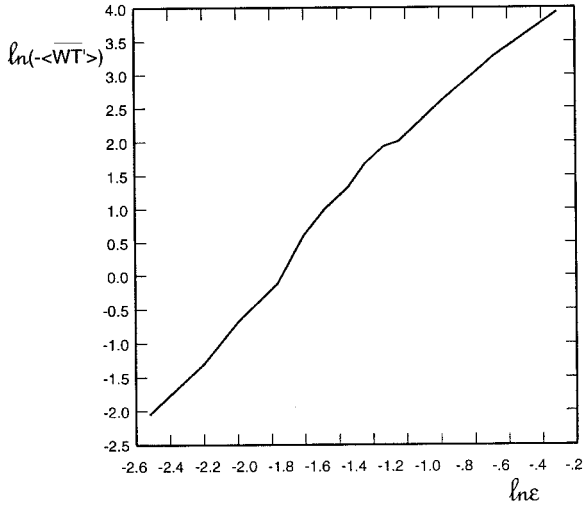

Figure 20. The statistically averaged (for each R) value of the heat flux plotted as a function of ϵ in the logarithmic coordinates (see text). The plot is almost a straight line which confirms the (assumed) relationship (34). The slope of this line is conveniently used to estimate the scaling of the heat flux in terms of ϵ.

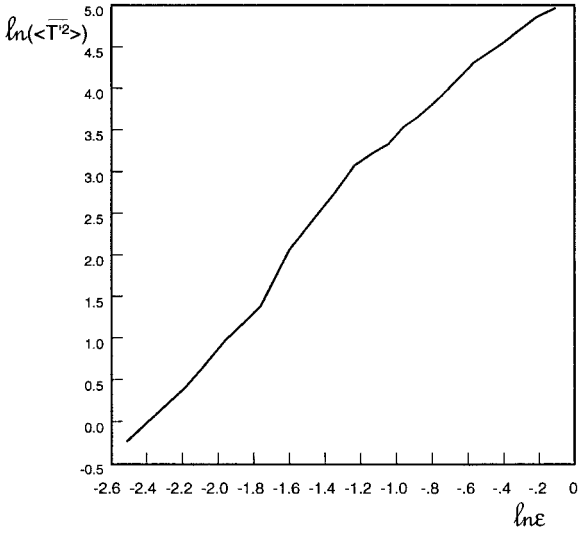

Figure 21. The same diagnostic as in Figure 21 is performed for the temperature variance av$\overline{\langle T'^2 \rangle}$.

approximate formula for the heat flux is

$$\text{Nusselt number} \cong 70\epsilon^{2.5}, \qquad (0.07 < \epsilon < 0.8).$$

It is important to note that at $R = 1.6$ this number already is much greater than unity, and that $R = 1.6$ is actually very "far" from the near neutral $R \to 1$ at which a more intense convection is expected leading to the formation of sheets and (convecting) layers (Stern and Turner, 1969). In order to realize $R \to 1$ numerically it will be necessary to include much longer horizontal wavelengths. It is also suggested that a *three* dimensional perturbation be introduced, in order to explain the observed horizontal planform of the fingers.

Finally, we remark that our extraordinarily low Reynolds number (when $\epsilon \to 0$ and $\kappa_T/\nu \to 0$) calculations exhibit many features found in classical turbulence problems (shear flow at large Reynolds number, and thermal convection at very large Rayleigh number), such as the stochastic behavior of many modes interacting through their mean field modification [cf. β_T, β_S in (17)] and through the triad terms (③). It might therefore be possible to address some fundamental statistical issues in "turbulence" (e.g., the ergodic hypothesis) in the more accessible $\kappa_T/\nu \to 0$, $\epsilon \to 0$ parametric regime of the salt finger problem.

Acknowledgment. This work was begun at the Geophysical Fluid Dynamics Summer Program at the Woods Hole Oceanographic Institution and supported by the National Science Foundation.

APPENDIX

Steady state, two-dimensional amplitude approximation for $\epsilon \ll 1$

To complete the steady state finite amplitude calculation mentioned at the end of Section 2a, we substitute the steady versions of Eq. (4), viz.,

$$\partial\theta/\partial z = \overline{wT'} - \langle\overline{WT'}\rangle, \tag{A1}$$

$$\partial\sigma/\partial z = \tau^{-1}\overline{WS'} - \tau^{-1}\langle\overline{WS'}\rangle, \tag{A2}$$

into Eq. (8), along with the steady operators $\mathbf{D} = \mathbf{D}_\tau = \nabla^2$, $\mathbf{L} = \mathbf{L}(0, \partial/\partial x, \partial/\partial z)$. For small ϵ and λ_m (Eq. (11)), the latter operator may be expanded as

$$\mathbf{L}(0, \ldots) = L(\lambda_m, \ldots) - \lambda_m \partial\mathbf{L}(0, \ldots)/\partial\lambda_m + \ldots,$$

where

$$\partial\mathbf{L}(0, \ldots)/\partial\lambda_m = -(1 + \tau^{-1})\nabla^6 - (\tau^{-1} - 1)\nabla_2^2. \tag{A3}$$

And Eq. (8) may then be written as

$$L\left(\lambda_m, \frac{\partial}{\partial x}, 0, \frac{\partial}{\partial z}\right)w = \lambda_m \frac{\partial L}{\partial \lambda_m}(w) + Q + N + \ldots \tag{A4a}$$

$$L\left(\lambda_m, \frac{\partial}{\partial x}, 0, \frac{\partial}{\partial z}\right)w = \lambda_m \frac{\partial L}{\partial \lambda_m}(w) + \tau^{-2}(\nabla_2^2\nabla^2 w)[\overline{wS}' - \langle\overline{wS}'\rangle] - \nabla_2^2\nabla^2 w[\overline{wT'} - \langle\overline{wT'}\rangle] + N + \ldots. \tag{A4b}$$

The total velocity w is the sum of the normal mode with amplitude A and all other Fourier modes w_2, i.e.,

$$w = Aw_m + w_2. \tag{A5}$$

An approximation to A can be obtained from the solubility condition for the inhomogeneous differential equation (A4b); to get this, Eq. (A4a) (or (A4b)) is multiplied by w_m and then integrated. Since the self adjoint linear operator satisfies $L(\lambda_m, \ldots)w_m = 0$ we get $\langle\overline{w_m L w}\rangle = 0$ for the left-hand side of A4a (A4b), and thus the solvability condition is

$$\left\langle\overline{w_m \frac{\partial \mathbf{L}}{\partial \lambda_m}(0, \ldots)w_m}\right\rangle + \langle\overline{w_m Q}\rangle + \langle\overline{w_m N}\rangle = 0. \tag{A6}$$

Since w must vanish as $\epsilon \to 0$, we tentatively assume that the temporal evolution of the initial disturbance consisting of the normal mode (w_m) leads to a steady state in which the nonlinearly generated w_2 harmonics in (A5) have relatively small value, i.e., $w_2 \gg Aw_m$; this is equivalent to a single mode (Galerkin) truncation. When w is replaced by Aw_m in

(A6) it is easily shown that $N \equiv 0$ (Malkus and Veronis, 1958). In the remaining equation

$$\left\langle \overline{w_m \frac{\partial \mathbf{L}}{\partial \lambda_m}(Aw_m)} \right\rangle + \langle \overline{w_m Q} \rangle = 0$$

the T', S' terms in Q (Eq. (A4b)) are replaced by $-(k_0^2 + m^2)^{-1} A w_m$, according to the $\epsilon \to 0$ approximation (12) for the normal mode. We then get an algebraic equation for A whose coefficients contain the wave-numbers, or their rescaled values as given by Eqs. (10b,c). After some trigonometric and algebraic manipulation we obtain the result

$$A^2 = \frac{8\epsilon^{3/2}}{(\tau^{-2} - 1)} \frac{\hat{k}^2 + \hat{m}^2}{\hat{k}^2} [\hat{k}^2 - (\hat{k}^2 + \hat{m}^2)^3], \tag{A7}$$

and for long fingers $\hat{m}^2/\hat{k}^2 \ll 1$, $\hat{k}^2 = 1/\sqrt{3}$ this becomes

$$A^2 = \frac{16}{3\sqrt{3}} \left[\frac{1}{R\tau} - 1 \right]^{3/2} (\tau^{-2} - 1)^{-1}. \tag{A8}$$

Eq. (A8) is notable because it contains no adjustable parameters, and because it is quite finite, (unlike the solution for the $\partial/\partial z \equiv 0$ mode mentioned in Section 1). Unfortunately this result (A8) is not asymptotic for $\epsilon \to 0$, the reason being that the order of magnitude of the linear operator (9a) is small (in ϵ), so that the iterative procedure (not shown here) yields a value w_2 which is of the same order (in ϵ) as Aw_m (see Eq. A5). Nevertheless, Section 3a shows that the mode truncation approximation (A7) is quite useful for explaining the amplitude for *moderate* $\hat{m}/\hat{k} = O(1)$, where the higher harmonics (e.g., $3\hat{m}$) are numerically smaller.

REFERENCES

Canuto, C., M. Y. Hussaini, A. Quarteroni and T. A. Zang. 1987. Spectral Methods in Fluid Dynamics, Springer Series in Computational Physics. Springer-Verlag, 567 pp.

Carmack, E. C., R. W. Macdonald, R. G. Perkin, F. A. McLaughlin and R. J. Pearson. 1995. Evidence for warming of Atlantic water in the southern Canadian Basin of the Artic Ocean. Geophys. Res. Lett., *22,* 1061–1064.

Holyer, J. Y. 1984. The stability of long steady, two dimensional salt fingers. J. Fluid Mech., *147,* 169–185.

Joyce, T. M. 1982. Marginally unstable salt fingers: Limits to growth. J. Mar. Res., *40,* Supplement 291–306.

Kunze, E. 1994. A proposed flux constraint for salt finger in shear. J. Mar. Res., *52,* 999–1016.

Malkus, W. V. R. and G. Veronis. 1958. Finite amplitude cellular convection. J. Fluid Mech., *4,* 225–261.

Özgökmen, T. M., O. E. Esenkov and D. B. Olson. 1998. A numerical study of layer formation due to fingers in double-diffusive convection in a vertically-bounded domain. J. Mar. Res., *56,* (in press).

Proctor, M. R. E. and J. Y. Holyer. 1986. Planform selection in salt fingers. J. Fluid Mech., *168,* 241–253.

Ruddick, B. 1992. Intrusive mixing in a salt lens. J. Phys. Oceanogr., *22,* 1274–1285.

Ruddick, B. and D. Walsh. 1995. Observations of density perturbations which drive thermohaline intrusions, *in* Double Diffusive Convection, A. Brandt and H. Fernando, eds., Geophysical Monograph *94,* 329–334.

Schmitt, R. W., H. Perkins, J. D. Boyd and M. C. Stalcup. 1987. C-SALT: An investigation of the thermohaline staircase in the western tropical North Atlantic. Deep-Sea Res., *34,* 1655–1666.

Shen, C. Y. and G. Veronis. 1997. Numerical simulation of two-dimensional salt fingers. J. Geophys. Res., *102,* 23131–23144.

Shirtcliffe, T. G. L. and J. S. Turner. 1970. Observations of the cell structure of salt fingers. J. Fluid Mech., *41,* 707–719.

Stern, M. E. 1975. Ocean Circulation Physics, International Geophysics Series, *19,* Academic Press, 246 pp.

Stern, M. E. and J. S. Turner. 1969. Salt fingers and convecting layers. Deep-Sea Res., *16,* 497–511.

Taylor, J. R. 1993. Anisotropy of salt fingers. J. Phys. Oceanogr., *23,* 554–565.

Turner, J. S. 1978. Double diffusive intrusions into a density gradient. J. Geophys. Res., *83,* 2887–2901.

Whitfield, D. W. A., G. Holloway and J. Y. Holyer. 1989. Spectral transform simulations of finite amplitude double-diffusive instabilities in two dimensions. J. Mar. Res., *47,* 241–265.

Williams, A. J. 1981. The role of double diffusion in a Gulf Stream front. J. Geophys. Res., *86,* 1917–1928.

Received: *12 September, 1996;* revised: *23 September, 1997.*